AEDC-TR-70-231

cy 2

IONIZATIONAL AND THERMAL NONEQUILIBRIUM IN MHD BOUNDARY LAYERS

Donald W. Cott

ARO, Inc.

November 1970

PROPULSION WIND TUNNEL FACILITY
ARNOLD ENGINEERING DEVELOPMENT CENTER
AIR FORCE SYSTEMS COMMAND
ARNOLD AIR FORCE STATION, TENNESSEE

NOTICES

When U. S. Government drawings specifications, or other data are used for any purpose other than a definitely related Government procurement operation, the Government thereby incurs no responsibility nor any obligation whatsoever, and the fact that the Government may have formulated, furnished, or in any way supplied the said drawings, specifications, or other data, is not to be regarded by implication or otherwise, or in any manner licensing the holder or any other person or corporation, or conveying any rights or permission to manufacture, use, or sell any patented invention that may in any way be related thereto.

Qualified users may obtain copies of this report from the Defense Documentation Center.

References to named commercial products in this report are not to be considered in any sense as an endorsement of the product by the United States Air Force or the Government.

IONIZATIONAL AND THERMAL NONEQUILIBRIUM IN MHD BOUNDARY LAYERS

Donald W. Cott
ARO, Inc.

FOREWORD

The work reported herein was sponsored by Headquarters, Arnold Engineering Development Center (AEDC), Air Force Systems Command (AFSC), under Program Element 64719F.

The results of the research presented were obtained by ARO, Inc. (a subsidiary of Sverdrup & Parcel and Associates, Inc.), contract operator of AEDC, AFSC, Arnold Air Force Station, Tennessee, under Contract F40600-71-C-0002. The investigation was conducted under ARO Projects PW3818 and PW3018 from July 1, 1968 to June 30, 1969, and the manuscript was submitted for publication on May 1, 1970.

This technical report has been reviewed and is approved.

Thomas G. Horn
First Lieutenant, USAF
Directorate of Civil
Engineering

Ernest F. Moore
Colonel, USAF
Director of Civil
Engineering

ABSTRACT

The effects of thermal nonequilibrium (elevated electron temperature) and ionizational nonequilibrium (finite-rate recombination) are studied in the insulator boundary layer of a potassium-seeded nitrogen MHD accelerator flow. The nonsimilar, compressible boundary layer is assumed steady, laminar, and two-dimensional. A collisionless sheath is assumed and matched with the boundary layer equations, which are solved numerically for a core flow Hall-neutralized Faraday accelerator. The relative importance of the various terms in the electron energy equation are assessed, and the overall effect of the nonequilibrium phenomena on the boundary layer parameters is described. It is concluded that thermal nonequilibrium can lead to significant B-wall shorting in long channels and that Hall effects should not be neglected but that operation is not noticeably affected by ionizational nonequilibrium or the physics of the electrostatic sheath.

CONTENTS

APPENDIX
Illustrations

NOMENCLATURE

A	Coefficient in linearized equations, given in Eq. (60)
$A_{es}^{(2)}$, $A_{es}^{(5)}$	Coefficients in Eq. (24), defined in Ref. 10
a	Generalized Conduction coefficient in Eq. (54)

B	Coefficient in linearized equations, given by Eq. (61)
$\vec{B}$	Magnetic field intensity, in channel flow coordinate system $\vec{B} = B(x)\,\tilde{k}$
b	Generalized source term in Eq. (54)
C	Coefficient in linearized equations, given by Eq. (62), also used for generalized conduction coefficient in Eq. (51)
C_e^*	Saha equilibrium electron concentration, given by Eq. (11)
C_f	Skin friction coefficient, $C_f \equiv \frac{\tau}{1/2\,\rho u_\infty^2}$
C_K^*	Potassium neutral concentration at Saha equilibrium
C_{K_0}	Original potassium seed mass concentration
C_p	Specific heat of overall gas at constant pressure
C_{p_s}	Specific heat of species s at constant pressure, i.e., $h_s = C_{p_s} T_s$
C_s	ρ_s/ρ, mass concentration of species s
$\vec{c}_s$	$\vec{w}_s - \vec{v}$, thermal velocity with respect to mass averaged velocity
$\vec{c}_s'$	$\vec{w}_s - \vec{v}_s$, the instantaneous velocity of a particle of species s with respect to the mean velocity of that species, thus the random velocity due to thermal agitation, i.e., $\langle \vec{c}_s' \rangle = 0$
$d\bar{c}$	$dc_1 dc_2 dc_3$, an element of velocity space, where appropriate $d\bar{w}$ or $d\bar{c}$ may also be used to denote an element of velocity space
$d\bar{c}'$	$dc_1' dc_2' dc_3'$, an element of velocity space
$d\bar{w}$	$dw_1 dw_2 dw_3$, an element of velocity space
$\vec{E}$	Electric field strength, in channel flow coordinate system $\vec{E} = E_x\tilde{i} + E_y\tilde{j}$
e	Absolute charge on an electron
f_s	Non-normalized velocity distribution function for s species, i.e., $n_s = \int f_s\, d\bar{w}$
g_{rs}	Relative speed between particle r and particle s
g_5	$\frac{(a_{i+1} + a_i)}{(\omega_{i+1} - \omega_{i-1})(\omega_{i+1} - \omega_i)}$

g_6 $\dfrac{(a_i + a_{i-1})}{(\omega_{i+1} - \omega_{i-1})(\omega_i - \omega_{i-1})}$

H $h + v^2/2$, stagnation enthalpy

h $\sum_s C_s h_s$, static enthalpy

h_s $(1/m_s)\left\langle \epsilon^s_{int} + 1/2\ m_s c_s^2 \right\rangle + p_s/\rho_s$, static enthalpy of species s

$\tilde{i}, \tilde{j}, \tilde{k}$ Unit vectors in orthogonal (x, y, z) coordinate system, (~) is used to avoid confusion with $\vec{j}$, the current density, and with i, j, and k when used as dummy indices

$\vec{J}$ $\sum_s \vec{J}_s$, total current density

$\vec{J}_s$ $\vec{J}_s + q_s n_s \vec{v}$, total current due to species s, sum of conducted current and convected current

$\vec{j}$ $\sum_s \vec{j}_s$, net conducted current

$\vec{j}_s$ $q_s n_s \vec{V}_s$, conduction current density carried by species 2

K_s Equilibrium constant, $n_i n_e/n_K = 2.41 \times 10^{21}\ T_e^{3/2}\ Z_{rs}\ e^{-50,408./T_e}$

k Boltzmann's constant

κ_e Electron thermal conductivity

ℓ Channel semi-width in direction of B-field, a function of x

m^*_{rs} Reduced mass

m_s Rest mass of a single particle of species s

n_s Number density of particles of species s, i.e., $n_s = \int f_s\, d\bar{w}$

Pr Prandtl number

P_1 $\dfrac{(\omega_{i+1} - \omega_i)}{4(x_D - x_U)(\omega_{i+1} - \omega_{i-1})}$

P_2 $\dfrac{3}{4(x_D - x_U)}$

P_3 $\dfrac{(\omega_i - \omega_{i-1})}{4(x_D - x_U)(\omega_{i+1} - \omega_{i-1})}$

p Scalar pressure $p = \sum_s p_s$

p_s $\frac{1}{3} \sum_{i=1}^{3} \rho_s \left\langle c_i c_i \right\rangle_s = \frac{1}{3} \rho_s \left\langle c^2 \right\rangle_s = n_s k T_s$, the scalar pressure of species s, which is defined as the trace of $\overleftrightarrow{p}_s$

Q_{sr}	Collision cross section between species s and species r
$\vec{q}$	$\sum_s \vec{q}_s$, total heat transfer
$\vec{q}_s$	$n_s \left\langle c_s \left(1/2\, m_s c_s^2 + \epsilon_{int}^s\right)\right\rangle_{s'}$ heat transfer carried by species s
q_s	Electric charge on a particle of species s
R	Overall gas constant
S	Generalized source term in Eq. (51)
T	Temperature of the heavier components of the gas
T_s	Temperature of species s
u, v, w	Mass averaged velocity in x-, y-, and z-directions, respectively
$\vec{V}_s$	$\vec{v}_s - \vec{v}$, average drift velocity of species s $\vec{V}_s = \vec{v}_s - \vec{v} = \vec{v} + \langle\vec{c}\rangle_s - \vec{v} = \langle\vec{c}\rangle_s$
$\vec{v}$	$\frac{1}{\rho}\sum_s \rho_s v_s$, mass averaged velocity $\vec{v} = u\tilde{i} + v\tilde{j} + w\tilde{k}$ in channel coordinate system
$\vec{v}_s$	Species average velocity, i.e., $\vec{v}_s = \langle\vec{w}\rangle_s = \frac{1}{n_s}\int f_s \vec{w}_s \, d\vec{w}$
$\vec{w}_s$	Instantaneous velocity of a given particle with respect to laboratory coordinates
x, y, z	Channel flow cartesian coordinate system, x is aligned with the primary flow, y is normal to the electrode walls, and z is normal to the insulator walls
Z	Compressibility factor
Z_{rs}	Partition function = $Z_i Z_e / Z_K$ $Z_{rs} = 9.11 \times 10^{-1} + 7.33 \times 10^{-5}\, T - 1.49 \times 10^{-8}\, T^2$
α_{rec}	Recombination rate coefficient
β	Hall parameter, $\beta = \sigma_e B/n_e e$
$\vec{\Gamma}_s$	$\equiv n_s \vec{V}_s$ = diffusion flux of species s
Δ'	Correction factor for the electrical conductivity of a multicomponent plasma, which takes thermal nonequilibrium into account, see Eq. (24)
$\Delta\phi$	Potential difference across sheath

δ Boundary layer thickness at $u/u_\infty = 0.95$

δ_{eff} Effective energy-loss factor, see Eq. (33)

δ^* Displacement boundary layer thickness

$$\delta^* = \int_0^\infty \left(1 - \frac{\rho u}{\rho_\infty u_\infty}\right) dz$$

δ_s A multiplying factor included in the energy collision integral to account for inelastic collisions; for perfectly elastic particles $\delta_s = 1$

ϵ_o Permitivity of free space

ϵ^s_{int} Internal energy tied up in an individual s particle

ϵ^s_{rec} Recombination energy of the ions of species s, (per particle) - this is treated in the formulation of the equations as a positive value

θ_v Characteristic vibration temperature

Λ Defined in Eq. (27)

λ_d Debye length, see Eq (28)

λ_e Electron-neutral mean-free-path, see Eq. (35)

μ Overall gas viscosity

ν_o Overall electron collision frequency, see Eq. (32)

ν^*_{sr} The effective momentum collision frequency between particles of the s and r species,

$$\nu^*_{sr} = \frac{n_r}{3n_s k T_s}\left(\frac{m_r m_s}{m_r + m_s}\right)\int Q_{sr}\, c_s'^3\, f_s\, d\bar{c}_s'$$

ρ $= \sum_s \rho_s$ = mass density

ρ_s $= m_s n_s = \int m_s f_s\, d\bar{w}$ = mass density of species s

$\dot{\rho}_s$ $\left(\frac{\partial \rho_s}{\partial t}\right)_{chem}$, shorthand notation for the collision term in the species conservation equation

σ_o Electrical conductivity, first order approximation

σ_s Electrical conductivity, second order approximation

τ Skin friction

ϕ Generalized dependent variable in Eq. (51)

ψ	Stream function
ψ_ℓ	Stream function at centerplane of channel
ψ_1	$\frac{4p}{K_s kT}$, a parameter in Saha's equation
ω	Normalized stream function, ψ/ψ_ℓ, see Eq. (52)

SUBSCRIPTS AND SUPERSCRIPTS

A, B	Halfway values between grid line i and the neighboring grid lines
D, U	Downstream and upstream stations, respectively
i	i^{th} component or a grid index
o	Denotes either initial value at channel entrance, or value at edge of sheath
r	Denotes some species other than s
s	The s in either subscript or superscript denotes species, it is moved up to the superscript position when there are other subscripts (e, electron; i, ion; N_2, nitrogen)
w	Denotes wall value
x, y, or z	Denotes component of a vector in the x, y, or z direction
∞	Denotes core flow value

SECTION I
INTRODUCTION

In recent years, a great deal of interest has been focused on the effects of elevated electron temperature and nonequilibrium recombination on the performance of magnetohydrodynamic (MHD) accelerators and generators. The problem is particularly acute for accelerators, where higher current densities tend to elevate the electron temperature, which in turn drastically affects the electrical conductivity. Hale and Kerrebrock (Ref. 1) and Sherman and Reshotko (Ref. 2) have examined the effects of elevated electron temperatures on insulator walls assuming equilibrium electron concentration throughout the boundary layer, as determined by Saha's equation evaluated at the electron temperature. For practical accelerators and generators, this Saha equilibrium assumption is adequate in the core flow and across most of the boundary layer. Near the wall, however, there is evidence which suggests that the electron concentration is governed by finite recombintation rates. In this case, the very strong coupling between electron temperature and electrical conductivity, through Saha's equation, is considerably modified. If this ionizational nonequilibrium extends very far out into the boundary layer, then the effect on the overall boundary layer might be significantly different than earlier analyses indicate.

The purpose of this study is to provide insight into the relative importance of elevated electron temperature and nonequilibrium recombination in typical accelerators. The flow in a typical Faraday accelerator is studied, using potassium seeded nitrogen as a working fluid. Only the insulator, or B-wall, is considered, since this is where the most potentially detrimental effects are expected to occur. To make the problem more tractable, steady, two-dimensional, laminar flow is assumed in the plane of the magnetic field. A nonsimilar, implicit, numerical technique is used to calculate the flow field in the continuum region, and this is carefully coupled to a relatively simple collisionless sheath model.

SECTION II
THEORETICAL FORMULATION

2.1 EQUATIONS OF MOTION

The procedure followed in the derivation of the equations of motion was the conventional multifluid formulation. The details of this approach

are presented in several standard references, but the most nearly applicable formulation, for the present purpose, is contained in Sutton and Sherman (Ref. 3). This formulation briefly consists of taking the mass, momentum, and energy moments of the Boltzmann equation for each species, thus yielding macroscopic equations describing the species behavior. This very general set of multifluid equations is then simplified in Ref. 4 to a two-fluid system of equations of boundary layer form. It is believed that this two-fluid system of equations adequately represents the nonequilibrium phenomena under study, while offering the advantage of being simple enough to be numerically tractable.

The major simplifying assumptions inherent in this analysis are summarized as follows:

1. Magnetic Reynolds number small (Maxwell's equations ignored),
2. Plasma quasi-neutral (except in sheath),
3. All species except electrons in thermal equilibrium,
4. Usual steady, laminar, two-dimensional boundary layer approximations valid,
5. Wall cold, fully catalytic, and a perfect electrical insulator,
6. Debye length smaller than or equal to the electron mean-free-path,
7. Three-dimensional swirl due to Hall current neglected,
8. Three-body recombination only, and
9. Radiation effects negligible.

The two-fluid formulation of the equations of motion is presented as follows:

Overall Continuity

$$\frac{\partial(\rho u)}{\partial x} + \frac{\partial(\rho w)}{\partial z} = 0 \tag{1}$$

Overall Momentum

$$\rho u \frac{\partial u}{\partial x} + \rho w \frac{\partial u}{\partial z} = - \frac{dp}{dx} + j_y B + \frac{\partial}{\partial z}\left(\mu \frac{\partial u}{\partial z}\right) \tag{2}$$

Overall Energy

$$\rho u \frac{\partial H}{\partial x} + \rho w \frac{\partial H}{\partial z} = \frac{\partial}{\partial z}\left[\frac{\mu}{Pr}\frac{\partial H}{\partial z}\right] + \frac{\partial}{\partial z}\left[\left(1 - \frac{1}{Pr}\right)\frac{\mu}{2}\frac{\partial (u^2)}{\partial z}\right]$$

$$+ j_x E_x + j_y E_y - \frac{\partial}{\partial z}\left\{\left[\frac{5k}{2}(T + T_e) + \varepsilon^i_{rec}\right]\Gamma_{e_z}\right\}$$

$$+ \frac{\partial}{\partial z}\left[k_e \frac{\partial T_e}{\partial z}\right] \tag{3}$$

Electron Diffusion

$$\rho u \frac{\partial C_e}{\partial x} + \rho w \frac{\partial C_e}{\partial z} = - \frac{\partial}{\partial z}\left[m_e \Gamma_{e_z}\right] + \dot{\rho}_e \tag{4}$$

Electron Energy

$$\rho u \frac{\partial T_e}{\partial x} + \rho w \frac{\partial T_e}{\partial z} = \frac{1}{C_e}\frac{\partial}{\partial z}\left[k_e \frac{\partial T_e}{C_{p_e}}\frac{\partial T_e}{\partial z}\right] - \frac{m_e \Gamma_{e_z}}{C_e}\frac{\partial T_e}{\partial z}$$

$$+ \frac{E_x J_{e_x} + E_y J_{e_y}}{C_e C_{p_e}} - \frac{3}{5}\left(\frac{e\rho}{m_e}\right)^2 \frac{C_e}{\sigma_o}\delta_{eff}(T_e - T)$$

$$- \left[T_e + \frac{2\varepsilon^i_{rec}}{5k}\right]\frac{\dot{\rho}_e}{C_e} + \frac{e\rho u j_{e_x}}{m_e C_{p_e} \sigma_o} \tag{5}$$

Equations (1) through (5) describe the boundary layer on the insulator wall of a typical accelerator channel, as illustrated in Fig. 1. The primary flow is in the x-direction, the imposed magnetic field (B-field) is in the z-direction, normal to the insulator wall, the primary electrical current flow is in the y-direction, and the Hall current flows in the x-direction. Equations (1) through (3) are basically the conventional boundary layer equations. In this two-fluid formulation, they describe the motion of the heavy components of the

gas, namely the nitrogen background gas, the potassium neutrals, and the potassium ions. In addition to the conventional boundary layer terms, they contain terms accounting for the MHD body force, the joule dissipation, the energy carried by electrons and ions diffusing down through the boundary layer toward the cold wall, and the energy conducted by the electron gas due to the electron temperature gradient.

Equations (4) and (5) are boundary layer equations which describe the electron gas boundary layer. Equation (4), the electron diffusion equation, is familiar to those who have worked with high temperature boundary layers involving species diffusion. The electron energy Eq. (5), by contrast, is not in such common use. In the mathematical formulation of Hale and Kerrebrock (Ref. 1), for example, the joule dissipation term was simply balanced off against the collision term. This was quite adequate in the free stream and outer boundary layer but may be inadequate near the cold wall where the conduction and diffusion terms dominate. The electron energy equation used by Sherman and Reshotko (Ref. 2) was analogous to Eq. (5) in degree of sophistication, but this sophistication was to some extent negated by their assumption of ionizational equilibrium.

Equations (1) through (5) include terms such as the current densities j_x and j_y, the electron diffusion flux Γ_{e_z}, the electron recombination rate $\dot{\rho}_e$, the pressure p, and the equilibrium electron concentration C_e^*. These are related to the dependent variables by the following auxiliary relations:

Ohm's Law

$$j_y = \frac{\sigma_e (E_y - uB) + \beta^2 j_{y_\infty} \frac{n_e}{n_{e_\infty}}}{1 + \cdot \beta^2} \tag{6}$$

$$j_x = \beta\, j_y \left[\frac{j_{y_\infty}}{j_y} \frac{n_e}{n_{e_\infty}} - 1 \right] \tag{7}$$

Ambipolar Diffusion

$$\Gamma_{e_z} = - \frac{m_e}{\rho e^2 C_e} \left[\frac{\sigma_e \sigma_i}{\sigma_e + \sigma_i} \right] \frac{\partial}{\partial z} \left[p_e + p_i \right] \tag{8}$$

Recombination

$$\dot{\rho}_e = \alpha_{rec} \frac{\rho^3 C_e}{m_e^2} \left[\frac{C_e^{*2}}{C_K^*} \left(C_{K_0} - \frac{m_K}{m_e} C_e \right) - C_e^2 \right] \qquad (9)$$

State

$$p = \rho Z R T \qquad \text{and} \qquad p_s = \frac{k}{m_s} \rho C_s T_s \qquad (10)$$

Saha Equilibrium

$$C_e^* = \frac{2m_e}{\psi_1 m_{N_2}} \left[\sqrt{1 + \psi_1 \frac{m_{N_2}}{m_K} C_{K_0}} - 1 \right] \qquad (11)$$

The notation used in the preceding equations is defined in the Nomenclature, while expressions are presented in Section 2.2 for the gas properties μ, Pr, Z, R, C_p, κ_e, α_{rec}, δ_{eff}, σ_e, and σ_i.

Equations (6) and (7) are Ohm's Law with the assumption that E_x is a constant through the boundary layer and has a value such that $j_x = 0$ in the free stream; i.e., the Hall current is neutralized in the free stream. Equation (8) is the ambipolar diffusion flux in the form given in Ref. 4. Equations (9), (10), and (11) can be found, for example, in Ref. 3.

The foregoing system of five partial differential equations, together with the auxiliary relations, the gas property relations in Section 2.2, and the one-dimensional continuity equation, forms a closed system in terms of the dependent variables, u, w, H, C_e, and T_e, and the independent variables x and z.

2.2 GAS PROPERTIES

Accurate evaluation of the gas properties is one of the most important prerequisites to successful MHD flow calculations. This is because all of the gas properties are affected by the current density j. The most strongly affected is the electrical conductivity σ_e, while j itself is proportional to σ_e. Thus any inaccuracy in the calculation of σ_e will feed back through j, to multiply the inaccuracy. For this reason a great deal of effort has been made to utilize the best available methods to calculate the gas properties.

The overall gas properties R, Pr, Z, C_p and μ are not greatly affected by the potassium seed and, therefore, are essentially the same as for pure nitrogen. R and Pr were assumed constant at values of 1776 ft^2/sec^2-°R and 0.75, respectively. The following expressions were used for the remaining overall gas properties:

$$Z = 1 + 276.6 \left[\frac{3.661 \times 10^{-3}\ T}{p}\right] .4964\ e^{-\frac{55,831.}{T}} \qquad (12)$$

$$\frac{C_p}{R} = 3.5 + 1.514 \times 10^{-5}\ T + e^{\frac{\theta_v}{T}} \left[\frac{\frac{\theta_v}{T}}{e^{\frac{\theta_v}{T}} - 1}\right]^2$$

$$+ (Z - 1) \left[1 + \left(T + 1.125 \times 10^5\right)\left(\frac{0.4964}{T} + \frac{55,831.}{T^2}\right)\right] \qquad (13)$$

$$\mu = \left[1.21 \times 10^{-5}\ \frac{lbm}{ft\text{-}sec}\right] \left[\frac{T}{300°K}\right]^{0.668} \qquad (14)$$

where T is in degrees Kelvin and p is in atmospheres. Equations (12) and (13) are due to Ring of ARO, Inc., and are valid within a pressure range from 0.1 to 1.0 atmosphere and a temperature range from 200 to 5000°K. Equation (14) is a curve fit to calculations by Baulknight (Ref. 5) and is accurate to within 3 percent from 300 up to 5000°K.

The three-body recombination reaction

$$K + e^- \rightleftharpoons K^+ + 2\ e^- \qquad (15)$$

is considered to be the dominant reaction in this analysis. The kinetics of this reaction have been studied by Curry (Ref. 6), Cool and Zukoski (Ref. 7), and Dugan (Ref. 8) for potassium and other alkali metals. Calculations from these references have been distilled by Demetriades of STD Corporation into the curve fit

$$\alpha_{rec} = 3.47 \times 10^{-20}\ T_e^{-4.765} \qquad (16)$$

for the recombination rate coefficient α_{rec}, where α_{rec} is in m^6/sec and T_e is in degrees Kelvin. This curve fit agrees well with Refs. 6, 7, and 8 up to 3500°K and closely approximates the results of Ref. 8 up to 8000°K.

The conductivity of a gas for species s is defined in the notation of Sutton and Sherman (Ref. 3) as

$$\sigma_s = \frac{n_s q_s^2}{\sum_r m_{sr}^* \nu_{sr}^*} \tag{17}$$

where m_{sr}^* is the reduced mass and ν_{sr}^* is the effective momentum collision frequency.

By evaluating Eq. (17) first for the potassium ions, the dominant resistance to the diffusion of ions through the partially ionized plasma is assumed to be collisions with diatomic nitrogen molecules. Accordingly, the summation in Eq. (17) is approximated as

$$\sum_r m_{ir}^* \nu_{ir}^* \approx m_{iN_2}^* n_{N_2} \left\langle g_{iN_2} \right\rangle \left\langle Q_{iN_2} \right\rangle \tag{18}$$

For Maxwellian velocity distributions of the ions and neutrals about the heavy species temperature, the average relative speed $\langle g \rangle$ between colliding particles is

$$\left\langle g_{iN_2} \right\rangle = \left\langle \left| \vec{w}_i - \vec{w}_{N_2} \right| \right\rangle = \left[\frac{8\ kT}{\pi\ m_{iN_2}^*} \right]^{1/2} \tag{19}$$

Weber and Tempelmeyer (Ref. 9) present integrated potassium ion-nitrogen cross sections which may be approximated by the curve fit

$$Q_{iN_2} \approx 2.39 \times 10^{-17}\ T(1.756 \times 10^{-5}\ T - 0.5) \tag{20}$$

where T is in degrees Kelvin and Q_{iN_2} is in meters^2. Equations (17) through (20) then combine to yield the ion conductivity

$$\sigma_i = \frac{e^2}{2.39 \times 10^{-17}} \left[\frac{\pi}{8k\ m_{iN_2}^*} \right]^{1/2} \frac{n_e}{n_{N_2}}\ T^{-1.756 \times 10^{-5} T} \tag{21}$$

Evaluating Eq. (17) for the electrons is not nearly so simple because, for partially ionized plasmas, no single interaction predominates. Thus it is necessary to account for electron-neutral collisions, electron-ion collisions, and electron-electron interactions. This has been done in a very general formulation by Demetriades and Argyropoulos (Ref. 10) over the entire range of molar ionization fraction above 10^{-7}. This expression is

$$\sigma_e = \frac{\sigma_o}{1 - \Delta'} \tag{22}$$

where

$$\sigma_o = \frac{3}{4} \frac{n_e e^2}{m_e \left(\frac{8k T_e}{\pi m_e}\right)^{1/2} \sum_{s \neq e} n_s Q_{es}} \tag{23}$$

$$\Delta' = \frac{2.5 \left[\sum_{s \neq e} A_{es}^{(2)} n_s Q_{en}\right]^2 \Big/ \sum_{s \neq e} n_s Q_{es}}{\frac{2\sqrt{2}}{5} \left[1 - (2 \ell n \Lambda)^{-1}\right] n_e Q_{ei} + \Sigma A_{es}^{(5)} n_s Q_{es}} \tag{24}$$

$$Q_{es} = \frac{1}{2} \int_0^\infty Q_{es}^{(1)} t^2 e^{-t} dt \; ; \quad t = \frac{m_e c^2}{2k T_e} \tag{25}$$

$$Q_{ei} = \frac{\pi}{2} \left[\frac{e^2}{4\pi\varepsilon_o} \frac{1}{k T_e}\right]^2 \ell n \Lambda \tag{26}$$

$$\Lambda = 3\lambda_d \left[\frac{4\pi\varepsilon_o}{e^2}\right] k T_e \tag{27}$$

$$\lambda_d^{-2} = \frac{1}{\varepsilon_o} \sum_s \frac{n_s q_s^2}{k T_s} \tag{28}$$

The foregoing expressions are only as good as the cross sections, Q_{es}, which are used in them. In this study, the integrated collision cross sections used by Garrison (Ref. 11) are adopted as follows:

$$Q_{eK} = 4.0 \times 10^{-18} \tag{29}$$

$$Q_{eN_2} = 4.5565 \times 10^{-20} + 2.81786 \times 10^{-23} T_e - 4.99704 \times 10^{-27} T_e^2 + 3.30643 \times 10^{-31} T_e^3 \tag{30}$$

where Q_{eK} and Q_{eN_2} are in meters^2, and T_e is in degrees Kelvin. Equation (30) is a curve fit based on data collected by Shkarofsky, Bachynski, and Johnston (Ref. 12). Garrison (Ref. 11) has experimentally verified the accuracy of Eq. (22) when used with Eqs. (29) and (30) for near-equilibrium potassium-seeded nitrogen.

The electron thermal conductivity κ_e can be expressed from the results of Demetriades and Argyropoulos (Ref. 10) as

$$k_e = \left[\frac{ek}{m_e} \frac{n_e}{\nu_o}\right]^2 T_e \left[\frac{1}{\sigma_o} - \frac{1}{\sigma_e}\right] \tag{31}$$

where

$$\nu_o = \left(\frac{8k\ T_e}{\pi m_e}\right)^{1/2} \left[-\frac{4}{5} n_e\ Q_{ei} + \frac{4}{15} n_{N_2}\ Q_{eN_2} + \frac{4}{15} n_K\ Q_{eK}\right] \tag{32}$$

and σ_e, σ_o, Q_{ei}, Q_{eK}, and Q_{eN_2} are given in Eqs. (22), (23), (26), (29), and (30), respectively.

The average energy-loss factor, δ_{eff}, which accounts for inelastic collisions in the collision term of Eq. (5), may be defined in the notation of Sutton and Sherman (Ref. 3) as

$$\delta_{eff} \equiv \frac{\sum_s \frac{2m_e}{m_s} \delta_s\ \nu_{es}^*}{\sum_s \nu_{es}^*} = \frac{m_e \sigma_o}{n_e e^2} \sum_s \frac{2m_e}{m_s} \delta_s\ \nu_{es}^* \tag{33}$$

where δ_s is the energy-loss factor for the s species, as contrasted to δ_{eff} which is averaged over all the species. For perfect elastic collisions between electrons and particles of species s, $\delta_s = 1.0$. The use of δ_{eff} offers the advantage that it can be evaluated experimentally without detailed knowledge of the various species densities and the momentum cross sections. Experiments have been carried out by Demetriades (Ref. 13), with diatomic nitrogen, which indicate that δ_{eff} remains approximately constant at about 7.0×10^{-4}, for N_2 temperatures from about 2800 to 5000°K. This corresponds to a δ_{N_2} of about 18. While the conditions of this experiment were by no means identical with those of the boundary layer problem under consideration, it is nevertheless felt that this is as reliable as any data currently available.

It should be pointed out that all of the electron gas properties are strongly dependent on empirical evaluation of the collision cross sections or energy-loss factors; thus any future work undertaken should be based on improved evaluations of these quantities as they become available.

2.3 BOUNDARY CONDITIONS

In channel entrance flows such as the one considered here, the free-stream boundary conditions on u, H, C_e, and T_e can be calculated by simply dropping the transverse terms from the linearized equations of motion. In this way, the downstream values of the dependent variables can be calculated explicitly in a way that is consistent with the boundary layer calculation, which is implicit in the z-direction and explicit in the x-direction.

The wall boundary conditions are straightforward for the overall gas and are specified as

$$z \to 0 \Rightarrow \begin{cases} u \to 0 \\ w \to 0 \\ H \to H_w(x) \end{cases} \tag{34}$$

The wall boundary conditions for the electron gas properties, C_e and T_e, cannot be specified in a straightforward way because of the presence of the electrostatic sheath. This is considered in the next section.

2.3.1 Sheath Analysis

The physics of the electrostatic sheath is determined by the following assumptions:

1. Wall fully catalytic, perfect electrical insulator,
2. Debye length ≤ electron mean-free-path, (collisionless sheath), and
3. Electron and ion distributions Maxwellian about their respective temperatures.

Of the foregoing sheath assumptions, the second is the most restrictive for the present purposes. The electron mean-free-path λ_e near the wall may be approximated by

$$\lambda_e \approx \frac{\langle g_{eN_2} \rangle}{\nu^*_{eN_2}} = \frac{1}{n_{N_2} Q_{eN_2}} \tag{35}$$

while the Debye length λ_d is given by Eq. (28). These two equations may be combined to yield

$$\frac{\lambda_d}{\lambda_e} \approx n_{N_2} Q_{eN_2} \left[\frac{k\varepsilon_o T T_e}{n_e e^2 (T_e + T)} \right]^{1/2} \tag{36}$$

where $\lambda_d/\lambda_e \leq 1$ from assumption number two. In a typical potassium-seeded nitrogen accelerator with inlet core flow conditions of

$$\begin{aligned} p &\approx 1.\ \text{atm} \\ T &\approx T_e \approx 3500°K \\ C_e &\approx C_e^* \approx 10^{-8} \end{aligned} \tag{37}$$

the prevailing conditions near the insulator wall might reasonably be expected to be about

$$\begin{aligned} p &\approx 1.\ \text{atm} & C_e^* &\approx 10^{-20} \\ T &\approx 300.°K & C_e &\approx 10^{-12} \\ T_e &\approx 700.°K \end{aligned} \tag{38}$$

Evaluating Eq. (36) at the conditions of Eq. (38), using the cross section given by Equation (30), yields $\lambda_d/\lambda_e \approx 1$. Thus, the collisionless sheath assumption is somewhat marginal, and if subsequent calculations yield electron concentrations significantly smaller than 10^{-12}, this assumption will be invalidated.

The fully catalytic wall assumption means physically that no electrons or ions that reach the wall will bounce back without recombining. Since the wall is a perfect electrical insulator, the sheath potential will adjust itself such that equal fluxes of electrons and ions reach the wall. The thickness of the sheath is roughly one Debye length, the electron mean-free-path is assumed greater, hence the sheath is relatively collisionless.

The electron flux to the wall may be expressed as

$$\Gamma_{e_z} = \int f_e \, c_3 \, dc_1 dc_2 dc_3$$

where the limits on c_1 and c_2 are $-\infty$ to $+\infty$, but the limits on c_3 are $-\infty$ to $-[2e\Delta\phi/m_e]^{1/2}$. Since f_e is Maxwellian, this integrates to the expression

$$\Gamma_{e_z} = - n_e \left(\frac{k\,T_e}{2\pi m_e}\right)^{1/2} e^{-\frac{e\Delta\phi}{k\,T_e}} \tag{39}$$

The ion flux integral is similar, except that the limits on c_3 are $-\infty$ to 0, yielding for the ion flux

$$\Gamma_{i_z} = - n_e \left(\frac{k\,T}{2\pi m_i}\right)^{1/2} \tag{40}$$

Since the sheath potential drop, $\Delta\phi$, seeks a value which will equate the electron and ion flux, it may be expressed as

$$\Delta\phi = \frac{k\,T_e}{2e} \ln\left(\frac{T_e m_i}{T\,m_e}\right) \tag{41}$$

Combining Eqs. (39) and (41) yields the following expression for the electron flux across the sheath:

$$\Gamma_{e_o} = - \frac{\rho_o \, C_{e_o}}{m_e} \left(\frac{k\,T_o}{2\pi m_i}\right)^{1/2} \tag{42}$$

where the subscript o dentotes that a quantity is evaluated at the edge of the sheath. For the heavy gas properties these values are practically equal to the wall values, but for the electron gas they may be many orders of magnitude different from the wall values.

Equation (42) is one of two expressions which are used to describe the effect of the sheath. The other expression is the heat flux which is carried across the sheath by the electron gas. It is obtained in a similar way by expressing the electron energy flux as

$$q_{e_z} = \int \left(\frac{1}{2} m_e c_e^2\right) f_e \, c_3 \, dc_1 dc_2 dc_3$$

with the same limits as before. This integrates to

$$q_{e_z} = - \frac{\rho \, C_e}{2\sqrt{\pi}} \left[\frac{2k \, T_e}{m_e}\right]^{3/2} \left[\frac{e\Delta\phi}{2k \, T_e} + 1\right] e^{- \frac{e\Delta\phi}{k \, T_e}} \qquad (43)$$

Inclusion of Eq. (41) yields the final form of the electron heat flux across the sheath

$$q_{e_o} = - \frac{\rho_o \, C_{e_o} \, k \, T_{e_o}}{2m_e} \left[\frac{k \, T_o}{2\pi m_i}\right]^{1/2} \left[4 + \ell n\left(\frac{T_{e_o} \, m_i}{T_o \, m_e}\right)\right] \qquad (44)$$

Equations (42) and (44) may be used to define boundary conditions on C_e and T_e, if they are handled in such a way as to be compatible with the continuum boundary layer equations. This is accomplished through the use of a transition region, the physics of which is discussed in the next section.

2.3.2 Sheath-Continuum Compatibility

The transition region is herein defined as the region bordered by the collisionless electrostatic sheath on the wall side and the collision-dominated continuum flow which extends throughout most of the boundary layer and all of the core flow. The transition region is physically thin, extending from a normal distance of about one Debye length from the wall, to a distance of perhaps a thousand electron mean-free-paths. Each species within the transition region is assumed to be Maxwellian about its own temperature, collisional energy transfer between species becomes important with increasing normal distance, but electron-electron-ion collisions are infrequent enough to render recombination

effects negligible. The neutral gas properties are assumed constant at their wall values across the transition region, and convection terms are neglected. Current densities are assumed low enough for joule dissipation to be neglected.

With these assumptions, Eqs. (4) and (5), the electron diffusion and energy equations, become

$$\frac{d}{dz}\left[\Gamma_{e_z}\right] = 0 \tag{45}$$

and

$$\frac{dq_{e_z}}{dz} = -\frac{3\,C_{p_e}}{5}\left[\frac{e\rho}{m_e}\right]^2 \frac{C_e}{\sigma_o}\,\delta_{eff}\,(T_e - T) \tag{46}$$

where Γ_{e_z} is given by the ambipolar diffusion expression, Eq. (8), and

$$q_{e_z} = -k_e \frac{dT_e}{dz} + m_e h_e \Gamma_{e_z} \tag{47}$$

When the boundary conditions $C_e = C_{e_o}$ and $\Gamma_{e_z} = \Gamma_{e_o}$ at $z = 0$ are given, Eq. (45) can be integrated assuming that $\sigma_e >> \sigma_i$ and

$$\frac{dT_e}{dz} << \frac{dC_e}{dz}$$

This yields the following expression for the C_e profile across the transition region:

$$C_e \approx C_{e_o} + m\,z \tag{48}$$

where

$$m = -\Gamma_{e_o} \frac{e^2\,C_e}{k(T_e + T)\sigma_i} \tag{49}$$

which is approximately constant since $\sigma_i \sim C_e$ from Eq. (21), and T_e does not vary markedly from T_{e_o} across the transition region.

Equation (46), which describes the electron temperature variation across the transition region, is somewhat more difficult to handle, but

given the boundary conditions $T_e = T_{e_o}$ and $q_{e_z} = q_{e_o}$ at $z = 0$, it can be formally integrated as follows:

$$T_e = T_{e_o} - q_{e_o} \int_0^z \frac{dz}{k_e} + m_e \Gamma_{e_o} C_{p_e} \int_0^z \frac{T_e}{k_e} dz$$

$$+ \frac{3}{5} C_{p_e} \left[\frac{e\rho}{m_e}\right]^2 \delta_{eff} \int_0^z \frac{\int_0^z \frac{C_e^2}{\sigma_o} (T_e - T) dz}{k_e} dz \qquad (50)$$

This expression is integrated numerically across the transition region to yield values of T_e and dT_e/dz at the interface between the transition region and the collision-dominated outer boundary layer.

By using assumed values for C_{e_o} and T_{e_o}, Eqs. (48) and (50) are used to evaluate C_e, T_e, and their derivatives where the transition region merges into the boundary layer flow. These values then serve as mixed wall boundary conditions for Eqs. (4) and (5), the electron gas boundary layer equations.

The numerical method of solving the equations of motion coupled with the sheath dominated transition region equations is described in the next section.

SECTION III
NUMERICAL FORMULATION

3.1 PATANKAR-SPALDING TECHNIQUE

Equations (1) through (5), the boundary layer equations, were solved simultaneously using a numerical technique developed originally for turbulent flow by Patankar and Spalding (Refs. 14 and 15). This technique was chosen for several reasons, chief of which was the fact that it would facilitate the later extension of the solutions into the turbulent flow regime. Only the essential features of the Patankar-Spalding technique are discussed here, with the modifications that are required for this particular application. A much more general treatment is to be found in Ref. 14, whereas Ref. 15 is recommended for the details of the computer program.

The Patankar-Spalding technique takes advantage of the fact that Eqs. (1) through (5) share the common boundary layer form

$$\rho u \frac{\partial \phi}{\partial x} + \rho w \frac{\partial \phi}{\partial z} = \frac{\partial}{\partial z}\left[C \frac{\partial \phi}{\partial z}\right] + S \tag{51}$$

where ϕ is a generalized dependent variable, u, H, C_e, or T_e. This system of equations is solved in the normalized von Mises coordinate system, where ω is the cross-stream coordinate, defined by

$$d\omega = -\frac{\rho w}{\psi_\ell} dx + \frac{\rho u}{\psi_\ell} dz \tag{52}$$

where ψ_ℓ is the center plane stream function, a constant, defined by

$$\psi_\ell \equiv \int_0^\ell \rho u \, dz \tag{53}$$

In the transformed (x-ω) plane Eq. (1), the continuity equation, is automatically satisfied, and Eq. (51) assumes the form

$$\frac{\partial \phi}{\partial x} = \frac{\partial}{\partial \omega}\left[a \frac{\partial \phi}{\partial \omega}\right] + b \tag{54}$$

where $a \equiv \rho u/\psi_\ell^2 C$ and $b \equiv S/\rho u$. The expressions for a and b are given in Appendix D of Ref. 4 for the boundary layer equations, Eqs. (2) through (5).

By following Patankar and Spalding (Ref. 15), Eq. (54) is linearized by considering the shaded control volume in Fig. 2; ϕ is assumed to vary linearly in ω between the ω grid lines, with all ϕ values inside the control volume evaluated at the downstream station. With these assumptions in mind, the convection term is approximated as

$$\frac{\partial \phi}{\partial x} \approx \frac{\int_{x_U}^{x_D} \int_{\omega_A}^{\omega_B} \frac{\partial \phi}{\partial x} d\omega \, dx}{(x_D - x_U)(\omega_B - \omega_A)}$$

$$\approx P_1 \left(\phi_{i+1}^D - \phi_{i+1}^U\right) + P_2 \left(\phi_i^D - \phi_i^U\right) + P_3 \left(\phi_{i-1}^D - \phi_{i-1}^U\right) \tag{55}$$

where P_1, P_2, and P_3 are defined in the Nomenclature. The conduction term can be approximated as

$$\frac{\partial}{\partial\omega}\left[a\,\frac{\partial\phi}{\partial\omega}\right] \approx \frac{a_B^U\,\dfrac{\phi_{i+1}^D - \phi_i^D}{\omega_{i+1} - \omega_i} - a_A^U\,\dfrac{\phi_i^D - \phi_{i-1}^D}{\omega_i - \omega_{i-1}}}{\dfrac{1}{2}\left(\omega_{i+1} - \omega_{i-1}\right)}$$

$$\approx g_5\left(\phi_{i+1}^D - \phi_i^D\right) - g_6\left(\phi_i^D - \phi_{i-1}^D\right) \qquad (56)$$

where g_5 and g_6 are defined in the Nomenclature. The source term, b, is in most cases approximated by the expression

$$b^D \approx b_i^U + \left.\frac{\partial b}{\partial\phi}\right|_i^U \left(\phi_i^D - \phi_i^U\right) \qquad (57)$$

Under some circumstances, it is desirable to evaluate a particularly important source term to a higher degree of accuracy. Patankar and Spalding (Ref. 15) have suggested that this be done by extending the evaluation of the term to the adjacent two ω grid points. Here the source term b^D is assumed to vary linearly in ω between adjacent ω grid lines. The averaged b^D is then evaluated similarly to the convection term as follows:

$$b^D \approx \frac{\displaystyle\int_{x_U}^{x_D}\int_{\omega_A}^{\omega_B} b^D\,d\omega\,dx}{(x_D - x_U)\,(\omega_B - \omega_A)}$$

$$\approx \left[P_1 b_{i+1}^D + P_2 b_i^D + P_3 b_{i-1}^D\right](x_D - x_U) \qquad (58)$$

Equation (57) can then be substituted into Eq. (58) for an improved approximation to the source term.

It should be pointed out at this time that there are no hard and fast rules for the evaluation of source terms. Equations (57) and (58) are excellent guidelines, but their application often requires considerable

ingenuity. For example, the ionization term $\dot{\rho}_e$ in the electron diffusion Eq. (4) varies several orders of magnitude between adjacent ω-grid lines within the boundary layer. Since it is the dominant term in the electron diffusion equation throughout most of the boundary layer, one might consider using Eq. (58), supposedly a finer approximation than Eq. (57), to evaluate it. As it turns out, Eq. (58) yields a considerably poorer approximation due to the fact that it is dominated by the b^D_{i+1} term. Thus for exponentially varying source terms, a stepwise approximation is better than a linear one.

The linearized version of Eq. (54) may be obtained by substituting the approximate expressions Eqs. (55), (56), and (57) into Eq. (54), which yields, after some manipulation,

$$\phi_i^D = A\phi_{i+1}^D + B\phi_{i-1}^D + C \tag{59}$$

where

$$A = \frac{g_5 - P_1}{\left[P_2 + g_5 + g_6 - \left.\frac{\partial b}{\partial \phi}\right|_i^U\right]} \tag{60}$$

$$B = \frac{g_6 - P_3}{\left[P_2 + g_5 + g_6 - \left.\frac{\partial b}{\partial \phi}\right|_i^U\right]} \tag{61}$$

$$C = \frac{P_1\phi_{i+1}^U + P_2\phi_i^U + P_3\phi_{i-1}^U + b_i^U - \left.\frac{\partial b}{\partial \phi}\right|_i^U \phi_i^U}{\left[P_2 + g_5 + g_6 - \left.\frac{\partial b}{\partial \phi}\right|_i^U\right]} \tag{62}$$

where the coefficients A, B, and C are evaluated at the upstream station. Equation (58) could also have been used, resulting in slightly different coefficients in Eq. (59).

Once the boundary layer equations are linearized to the form of Eq. (59), it may be observed that the coefficients form a tridiagonal matrix. These matrices may be inverted in a straightforward way by

successive substitution to yield each succeeding downstream profile in ϕ. This procedure is described in detail in Patankar and Spalding (Ref. 15).

One of the most attractive features of the Patankar-Spalding technique is its use of Couette-flow assumptions near the wall. As Patankar and Spalding conceived it, the Couette-flow region is a computational necessity when used with their turbulent flow hypotheses. For laminar flow of the overall gas, the Couette-flow model is not necessary, as very little accuracy is lost by solving the linearized equations all the way to the wall. For the electron gas boundary layer, however, the Couette-flow concept offers a method of accurately coupling the mixed sheath boundary conditions to the linearized electron diffusion and energy equations. Here the transition region of Section 2.3 is treated as a Couette-flow region, and an iteration is performed between the Couette-flow solutions, Eqs. (48) and (50), and C_e and T_e boundary layer profiles. The iteration proceeds as follows: first C_{e_o} and T_{e_o} are set equal to their upstream values. Then Eqs. (48) and (50) are solved to yield T_e, dT_e/dz, C_e, and dC_e/dz at the outer edge of the transition, or Couette-flow, region. In general, these quantities are not equal to T_e, dT_e/dz, C_e, and dC_e/dz, evaluated at $\omega_{2.5}$, and the slip values and wall values of C_e and T_e are readjusted to bring them into equality. This readjustment yields new values for C_{e_o} and T_{e_o}, and the iteration is repeated until C_{e_o} and T_{e_o} no longer change in successive iterations.

While this iteration is cumbersome and expensive in computer time, it offers the distinct advantage that the boundary conditions need not be matched at the edge of the sheath, where continuum flow is a poor assumption. Rather, the boundary conditions are matched at something like a thousand electron mean-free-paths out from the wall, where the Patankar-Spalding technique is accurate, and the flow is still essentially continuum one-dimensional Couette-flow.

3.2 PRESSURE PREDICTION TECHNIQUE

In order to calculate the downstream velocity profiles, a pressure gradient, dp/dx, must be specified for the overall momentum equation, Eq. (2). Since the flow is confined, the pressure gradient cannot be specified a priori for a given area variation. This difficulty can be surmounted by several types of numerical schemes, all of which involve either assumptions regarding the variation of dp/dx, or iteration between dp/dx and the overall equations of motion. The latter techniques were rejected in this study because of the excessive computation time they

involve. Two methods of the former type were used, the first for a priori specified channel area variation, and the second for a priori specified temperature variation.

3.2.1 Specified Area Variation

A method due to Kitowski (Ref. 16) utilizes the upstream pressure gradient dp/dx in the overall momentum equation. Once the downstream velocity u and temperature T profiles are calculated, the downstream pressure is calculated using the integral continuity equation as follows:

$$d\omega = \frac{\rho u}{\psi_\ell}\, dz = \frac{p}{R\ \psi_\ell}\,\frac{u}{ZT}\, dz \tag{63}$$

where the equation of state, Eq. (10), and the definition of the normalized stream function, Eq. (52), have been included. Equation (63) can be integrated from the wall to the centerplane as follows:

$$p = \frac{R\ \psi_\ell}{\ell(x)} \int_0^1 \frac{ZT}{u}\, d\omega \tag{64}$$

to yield the downstream pressure as an integral function at the downstream u and T versus ω profiles, and the specified downstream channel semi-width $\ell(x)$. Once this downstream pressure is known, Eq. (63) may again be integrated to yield the z value corresponding to each ω value; i.e.,

$$z = \frac{R\ \psi_\ell}{p} \int_0^\omega \frac{ZT}{u}\, d\omega \tag{65}$$

Kitowski's method, although it fails to rigorously satisfy the momentum equation, yields satisfactory results for the flows under consideration here.

3.2.2 Specified Temperature Variation

Often it is desirable to design a channel configuration based on the a priori specification of certain properties down the channel. The case of near constant core flow temperature and current density is considered in detail in this investigation, since typical accelerator designs often

follow this process. For constant static temperature, Eqs. (2) and (3), the overall momentum and energy equations, may be reduced in the core flow to

$$\rho u \frac{du}{dx} = - \frac{dp}{dx} + j_y B \tag{66}$$

and

$$\rho u^2 \frac{du}{dx} = j_x E_x + j_y E_y \tag{67}$$

Equations (66) and (67) may then be combined to yield

$$u \frac{dp}{dx} = - j_x E_x + j_y (uB - E_y)$$

$$= - j_x \left[E_x - \frac{j_y B}{n_e e} \right] - j_y \left[E_y - uB + \frac{j_x B}{n_e e} \right]$$

therefore,

$$\frac{dp}{dx} = - \frac{j_x^2 + j_y^2}{u \sigma_e} \tag{68}$$

Equation (68) specifies the pressure gradient which is required for constant temperature one-dimensional flow. However, various anomalies arise in practice because of the presence of the rather thick boundary layers. These anomalies are accounted for by simply multiplying Eq. (68) by a correction factor (T/T_o) to an arbitrarily large power, thus

$$\frac{dp}{dx} = - \frac{\left(j_x^2 + j_y^2 \right)}{u \sigma_e} \left[\frac{T}{T_o} \right]^{50} \tag{69}$$

where T_o is the static temperature at the channel inlet. Then as the computation proceeds down the channel, if the temperature drifts away from T_o the pressure gradient is modified to keep the temperature nearly constant.

With the pressure gradient specified by Eq. (69), the downstream pressure is

$$p_D = p_U + \frac{dp}{dx}(x_D - x_U) \tag{70}$$

which yields sufficient information to evaluate Eq. (65) for the z values corresponding to each ω. It is useful to use this method of specified temperature variation to design a channel, and then proceed with the method of specified area variation to examine the channel performance for off-design conditions.

3.3 INITIAL PROFILES

The numerical computation is initiated upstream of the powered section of the channel in all cases. Thus at the initial station, MHD effects are negligible, and the overall gas profiles tend to be similar. Given arbitrary initial velocity and temperature profiles, which vary continuously between the correct boundary conditions, the profiles approach the correct similar solutions within the first five or six x-stations. Thus it is quite adequate, for the overall gas, to simply impose parabolic initial profiles and allow the numerical technique to march downstream for several integrations before entering the influence of the electric and magnetic fields. The electron temperature profile is equally simple to initiate, since the electron gas is in thermal equilibrium with the heavy species until it enters the electric field.

The initiation of the electron concentration profile is not so simple. It was found that if the C_e profile is initiated in Saha equilibrium, it takes approximately two hundred x-stations, or five feet, to asymptotically approach the correct C_e profile. This is because of the relatively low mobility of the ions in the ambipolar diffusion process by which the C_e profiles are filled in. With this in mind, the initial profiles for the powered accelerator section were computed by starting the computer program three hundred x-stations, or ten feet, upstream of the powered section. Three runs were made, corresponding to a recombination rate of zero (frozen flow), a physically realistic recombination rate as given by Eq. (16), and a near-equilibrium recombination rate given by Eq. (16) multiplied times 10^5. The resulting initial C_e profiles are plotted in Fig. 3. Note that on the linear scale in Fig. 3, the finite-rate and the near-equilibrium profiles appear identical, thus the boundary layer is essentially in ionizational equilibrium for the non-MHD case.

The initial velocity, gas temperature, and electron temperature profiles are discussed in Section 4.1.

SECTION IV
RESULTS

Computer calculations are discussed in detail in this section for the actual physical case, which involves the simultaneous presence of electron thermal nonequilibrium and ionizational nonequilibrium. The effects of varying the energy-loss factor (δ_{eff}) are presented, with a physically realistic recombination rate coefficient (α_{rec}). Then with a physically realistic δ_{eff}, the effects of varying α_{rec} are explored. Nonequilibrium calculations are also presented for the locally Hall-neutralized case, and compared with the results of the core flow Hall-neutralized calculations.

4.1 SIMULATANEOUS THERMAL AND IONIZATIONAL NONEQUILIBRIUM

In order to obtain a physically meaningful standard of comparison, the first channel flow solution was run with $\delta_{eff} = 7.0 \times 10^{-4}$ and α_{rec} as given by Eq. (16), which were felt to be the most realistic values currently available. The results of this computation are presented in Figs. 4 and 5. Figure 4a shows the geometry of the accelerator section, and the configuration of the electric and magnetic fields. The nature of the core flow was primarily determined by fixing the magnetic field (B), the transverse current density (j_{y_∞}), and the static temperature (T_∞), constant in the core flow throughout most of the channel, with B = 2.0 webers/m^2, j_{y_∞} = 15 amps/m^2, and T_∞ = 6300°R. The pressure variation and the area variation were determined by Eqs. (69) and (65), respectively, rather than being prescribed a priori. At the entrance of the channel, there were no fields present, with B being increased linearly from zero at $x/\ell_0 = 0$ to its full value at $x/\ell_0 = 10$. E_y was calculated from Ohm's law, assuming a linear buildup of j_{y_∞} to its full value at $x/\ell_0 = 10$. Throughout the channel, E_x was calculated by $E_x = \left[\frac{j_y B}{n_e e}\right]_\infty$, which kept the core flow Hall-neutralized ($j_{x_\infty} = 0$). The variations of core flow pressure, temperature, and velocity down the channel are plotted in Fig. 4b.

In Fig. 4c, several of the parameters which characterize the boundary layer are plotted down the channel. It should be emphasized at this point that no attempt to satisfy Maxwell's equations has been made. Therefore, the solutions presented in this investigation are not necessarily valid in the region where $0 \leq x/\ell_o \leq 10$. Thus the rather abrupt variation of C_f in the entrance should be disregarded. The δ which is plotted in Fig. 4c is the boundary layer thickness at the point where $u/u_\infty = 0.95$. Note the slight decrease in δ and δ^* near the channel exit. The reason for this is that boundary layer shorting developes near the end of the channel, and the resulting hump in the velocity profile results in a slight loss of mass in the velocity boundary layer. Local heat transfer rates are plotted in Fig. 4d. The increase in overall heat transfer (q) near the entrance should be ignored, but the increase near the exit is another significant result of the B-wall shorting effect. Note that the heat transfer rates for the ion (q_i) and electron (q_e) gases, while much smaller, are quite sensitive to the shorting phenomena. It is most significant that q_e and q_i are several orders of magnitude smaller than q. Considerably higher operating temperatures would be necessary for q_e and q_i to become important. The energy of recombination is arbitrarily assigned to the ions; this is why q_i is about an order of magnitude higher than q_e.

Figure 5 illustrates the development of the boundary layer profiles as they proceed down the channel. The initial profiles are represented by the first curve ($x/\ell_o = 0$) shown in each figure. The most important effect which is illustrated is the presence of B-wall shorting in about the last third of the channel. This is most evident in the current density profiles (Figs. 5c and d) which add vectorially to a maximum current density of 122 amps/cm^2 at $z/\delta = 0.34$ and $x/\ell_o = 120$. T_e and C_e (Figs. 5a and b) also display local maxima near the point of maximum current density. Thus Fig. 5 provides a picture of how B-wall shorting tends to amplify very quickly once it starts with j increasing T_e and C_e through joule heating, which in turn leads to higher σ and hence increased j. The influence of the shorting of transverse current may be seen in Fig. 5e, which shows the resulting velocity hump at the accelerator exit.

Although it is not evident from Figs. 4 and 5, the dominant terms in the electron energy equation for this case are the joule heating terms and the collision term, with the conduction and diffusion terms becoming important only in the region where $z/\delta \leq 0.05$. One of the reasons why conduction and diffusion are of little importance is that the electrostatic sheath tends to insulate the electron gas from the cold, fully catalytic wall. To illustrate this, at $x/\ell_o = 120$, the wall temperature is 530. °R, while the electron temperature at the outer edge of the

sheath, T_{e_o}, is 1940.°R. It is also interesting to note that at this point $C_{e_o} = 4.84 \times 10^{-14}$, as compared with a Saha equilibrium concentration at that point of 2.81×10^{-16}. While two orders of magnitude might seem like a great deal of ionizational nonequilibrium, this may be put in perspective by considering that it is less than 0.01 percent of the core flow electron concentration.

In Section 2.3, it was pointed out that the collisionless sheath model is invalid if C_{e_o} drops below 10^{-12}. Since $C_{e_o} = 4.84 \times 10^{-14}$, the sheath is in fact collision dominated from a thermal standpoint, although still frozen for the purpose of recombination. In order to check the implications of this violation of the collisionless sheath assumption,[1] the computer program was run with T_{e_o} and C_{e_o} set equal to their equilibrium wall values, 530°R and 3.29×10^{-39}, respectively. Surprisingly enough, the conduction and diffusion terms were still not strong enough to cause any significant change in the results in Figs. 4 and 5, outside a z/δ value of about 0.2. Thus, although the simple collisionless sheath model leaves much to be desired, it is adequate for the calculations presented herein.

4.2 ELECTRON THERMAL NONEQUILIBRIUM

To isolate the effects of electron thermal nonequilibrium, the computer program was run for the same case as in Section 4.1, except with different values of energy-loss factor. For this discussion, it is useful to use the species energy-loss factor, δ_s, which is related to the effective energy-loss factor, δ_{eff}, by Eq. (33). The physically realistic energy-loss factor is $\delta_{eff} \approx 7.0 \times 10^{-4}$, which corresponds to $\delta_{N_2} \approx 18$. The lowest value of δ_{N_2} which is reported in the literature is given as $\delta_{N_2} \approx 10.$, in Sutton and Sherman (Ref. 3). This lower energy-loss factor leads to much higher electron temperatures, and so a case was computed with this value. For the equilibrium extreme, δ_{N_2} was simply multiplied by a factor of 10^4 to yield $\delta_{N_2} \approx 1.8 \times 10^5$.

Figure 6 compares the boundary layer profiles for $\delta_{N_2} = 10$, 18, and 1.8×10^5, at $x/\ell_o = 82.0$. Smaller values of δ_{N_2} tend to severely aggravate the B-wall shorting problem, while no shorting at all exists for the case of electron thermal equilibrium ($\delta_{N_2} = 1.8 \times 10^5$). Keep in mind that these three cases were all run with the same recombination rate coefficient given by Eq. (16).

Figure 7 shows the effect of varying the energy-loss factor on two of the most important overall boundary layer parameters, δ^* and q. In both Figs. 7a and b, the $\delta_{N_2} = 18$ line is the same as in Figs. 4c and d. The plots for $\delta_{N_2} = 10$ are terminated beyond $x/\ell_o \approx 85$ because the electron temperature exceeded the range of validity of some of the assumptions used in evaluating the transport properties.

4.3 IONIZATIONAL NONEQUILIBRIUM

With a realistic energy-loss factor, the computer calculation of Section 4.1 was repeated twice more. This time with $\alpha_{rec} = 0$, to duplicate frozen recombination, and also with the α_{rec} given in Eq. (16) multiplied times 10^5, to duplicate near-equilibrium recombination. The resulting profiles are displayed in Fig. 8.

Note that C_e does remain very near to Saha equilibrium for all values of z/δ above 0.3. Recombination is essentially frozen then from about $z/\delta = 0.25$, on in to the wall. The frozen recombination profiles display no shorting because primarily σ is no longer coupled to T_e through C_e. The streamwise variation of the boundary layer parameters is not plotted since the physical case is so near the Saha equilibrium case.

4.4 LOCAL HALL-NEUTRALIZATION

It is not uncommon practice to neglect the effects of Hall currents when performing an analysis of nonequilibrium effects. This corresponds to local Hall-neutralization, where E_x at every point in the flow is assumed to have the value

$$E_x = \frac{j_y B}{n_e e} \tag{71}$$

such that no Hall current flows anywhere. Then Ohm's law becomes

$$j_y = \sigma (E_y - uB) \tag{72}$$

Such a procedure tends to overestimate the importance of electron thermal nonequilibrium, as is shown in Figs. 9 and 10. Here the computer results of Section 4.1 are compared with a similar computation

using Eqs. (71) and (72). The reason for this behavior may be seen from the simplified electron energy equation

$$\frac{3}{5} C_{p_e} \left[\frac{e\rho}{m_e}\right]^2 \frac{C_e^2}{\sigma_o} \delta_{eff} (T_e - T) = E_x j_{e_x} + E_y j_{e_y}$$

$$- n_e e u E_x + \frac{e n_e}{\sigma_o} u j_{e_x} \tag{73}$$

which results from Eq. (5) when all but the collision and joule dissipation terms are neglected. Consider the right hand side of Eq. (73) for the core flow Hall-neutralized case. Here $E_y j_{e_y}$ is the largest term, it is positive because both E_y and j_{e_y} are positive. E_x and u are positive, while j_{e_x} is negative. Thus, all three of the other terms, the Hall terms, on the right hand side are negative. So while the transverse current j_{e_y} is putting energy into the electron gas, the Hall terms are taking energy out. So, in effect, there is some Hall generation going on in the boundary layers of this Faraday accelerator. If the accelerator is run with local Hall-neutralization, then two of the negative Hall terms drop out, and $E_y j_{e_y}$ becomes much larger. Thus increasing the joule dissipation into the electron gas to an unrealistically high value.

Joule dissipation profiles are plotted for both types of Hall-neutralization in Fig. 9c. This form of the joule dissipation term may be developed from Equation (73) and using Ohm's law.

$$\frac{3}{5} C_{p_e} \left[\frac{e\rho}{m_e}\right]^2 \frac{C_e^2}{\sigma_o} \delta_{eff} (T_e - T) =$$

$$= j_{e_x}\left[E_x - \frac{j_{e_y} B}{n_e e}\right] + j_{e_y}\left[E_y + \frac{j_{e_x} B}{n_e e}\right] + e n_e u \left[\frac{j_{e_x}}{\sigma} - E_x\right]$$

$$= \frac{j_{e_x}^2}{\sigma_e} + j_{e_y}\left[E_y - uB + \frac{j_{e_x} B}{n_e e}\right]$$

$$= \frac{j_{e_x}^2 + j_{e_y}^2}{\sigma_e} = \frac{j^2}{\sigma_e} \tag{74}$$

The effects of local Hall-neutralization on the overall boundary layer parameters, δ^* and q, are shown in Fig. 10. Note that the severe boundary layer shorting brought on by local Hall-neutralization causes considerable overestimation of the heat transfer. Again, calculations for the locally Hall-neutralized case were terminated beyond $x/\ell_o = 35.2$ because of the high electron temperatures involved.

SECTION V
CONCLUSIONS

For the class of nitrogen accelerators under study here, nonequilibrium effects are of secondary importance in laminar boundary layers to an x/ℓ_o of about ninety, but beyond that point they are a direct cause of B-wall shorting. Once shorting begins, electron thermal nonequilibrium causes it to amplify very quickly, causing significant increases in heat transfer. If the channel is designed for equilibrium boundary layers, then the B-wall shorting is sufficient to cause thermal choking near the exit. Although there is considerable ionizational nonequilibrium in the colder portions of the boundary layer, it is insufficient in the hotter areas (where appreciable current flows) to affect the solutions noticeably. The relatively simple model of Hale and Kerrebrock (Ref. 1), which uses only the collision and joule heating terms in the electron energy equation and which assumed Saha equilibrium at the electron temperature, would have been quite adequate to describe the nonequilibrium effects for this application. Hall effects can be very important to the overall operation of a core flow Hall-neutralized device and should be neglected only if there is qualitative justification for it.

This study also points out the need for improved understanding of the basic collision phenomena involved in plasmas of engineering interest. For example, Figs. 6 and 7 demonstrate that the boundary layer behavior is very sensitive to the value of the energy-loss factor. While reliable energy-loss data are abundant for low temperature nitrogen and relatively high energy electrons, it is very scarce for higher temperature gases involving lesser degrees of thermal nonequilibrium. Thus it should be emphasized that these boundary layer calculations are only as good as the cross sections and energy-loss factors involved, and any future work undertaken should be based on improved evaluations of these quantities as they become available.

REFERENCES

1. Hale, F. J. and Kerrebrock, J. L. "Insulator Boundary Layers in MHD Channels." AIAA Journal, 2:461, March 1964.

2. Sherman, A. and Reshotko, E. "Nonequilibrium Boundary Layer along an Insulator Wall." AIAA Journal, 7:610, April 1969.

3. Sutton, G. W. and Sherman, A. Engineering Magnetohydrodynamics. New York: McGraw-Hill Book Company, Inc., 1965.

4. Cott, D. W. "Ionizational and Electron Thermal Nonequilibrium Effects in Compressible Magnetohydrodynamic Boundary Layers." PhD Thesis, University of Tennessee, Knoxville, Tennessee, December 1969.

5. Baulknight, C. W. "The Calculation of Transport Properties at Elevated Temperatures." Proceedings of the Second Biennial Gas Dynamics Symposium, A. B. Cambel and J. B. Fenn, editors. Evanston, Illinois: Northwestern University Press, 1958. pp. 89-95.

6. Curry, B. P. "Ionization and Recombination in Alkali-Seeded Collision-Dominated Plasmas." AEDC-TR-65-260 (AD627988). February 1966.

7. Cool, T. A. and Zukoski, E. E. "Recombination Rates and Non-equilibrium Electrical Conductivity in Seeded Plasmas." Physics of Fluids, 9:780, April 1966.

8. Dugan, J. V., Jr. "Three-Body Collisional Recombination of Cesium Seed Ions and Electrons in High-Density Plasmas with Argon Carrier Gas." National Aeronautics and Space Administration TND-2004, Washington, D. C., October 1964.

9. Weber, R. E. and Tempelmeyer, K. E. "Calculation of the D-C Electrical Conductivity of Equilibrium Nitrogen and Argon Plasma with and without Alkali Metal Seed." AEDC-TDR-64-119 (AD602858), July 1964.

10. Demetriades, S. T. and Argyropoulos, G. S. "Ohm's Law in Multicomponent Nonisothermal Plasmas with Temperature and Pressure Gradients." Physics of Fluids, 9:2136, November 1966.

11. Garrison, G. W. "Electrical Conductivity of a Seeded Nitrogen Plasma." AIAA Journal, 6:1264, July 1968.

12. Shkarofsky, I. P., Bachynski, M. P., and Johnston, T. W. "Collision Frequency Associated with High Temperature Air and Scattering Cross-Sections of the Constituents." Planetary and Space Science, Milton Greenberg, editor. Vol. 6. New York: Pergamon Press, 1961. P. 24.

13. Demetriades, S. T. "Determination of Energy-Loss Factors for Slow Electrons in Hot Gases." Physical Review, 158:215, June 10, 1967.

14. Patankar, S. V. and Spalding, D. B. "A Finite-Difference Procedure for Solving the Equations of the Two-Dimensional Boundary Layer." International Journal of Heat and Mass Transfer, 10:1389-1411, August 1967.

15. Patankar, S. V. and Spalding, D. B. Heat and Mass Transfer in Boundary Layers. Cleveland: CRC Press, 1968.

16. Kitowski, J. V. "Theory of Viscous Compressible Flow in a Slender Channel with Crossed Electric and Magnetic Fields." Ph.D. dissertation, The University of Tennessee, Knoxville, 1968.

APPENDIX
ILLUSTRATIONS

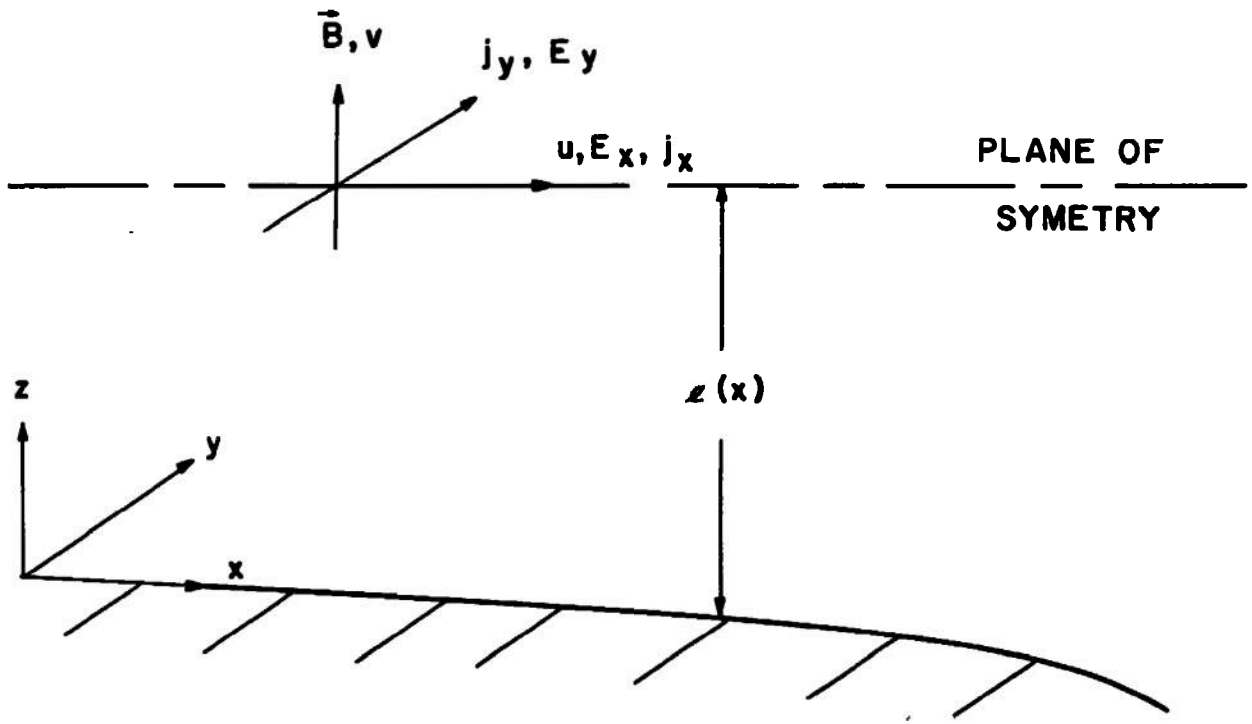

Fig. 1 Channel Flow Coordinate System

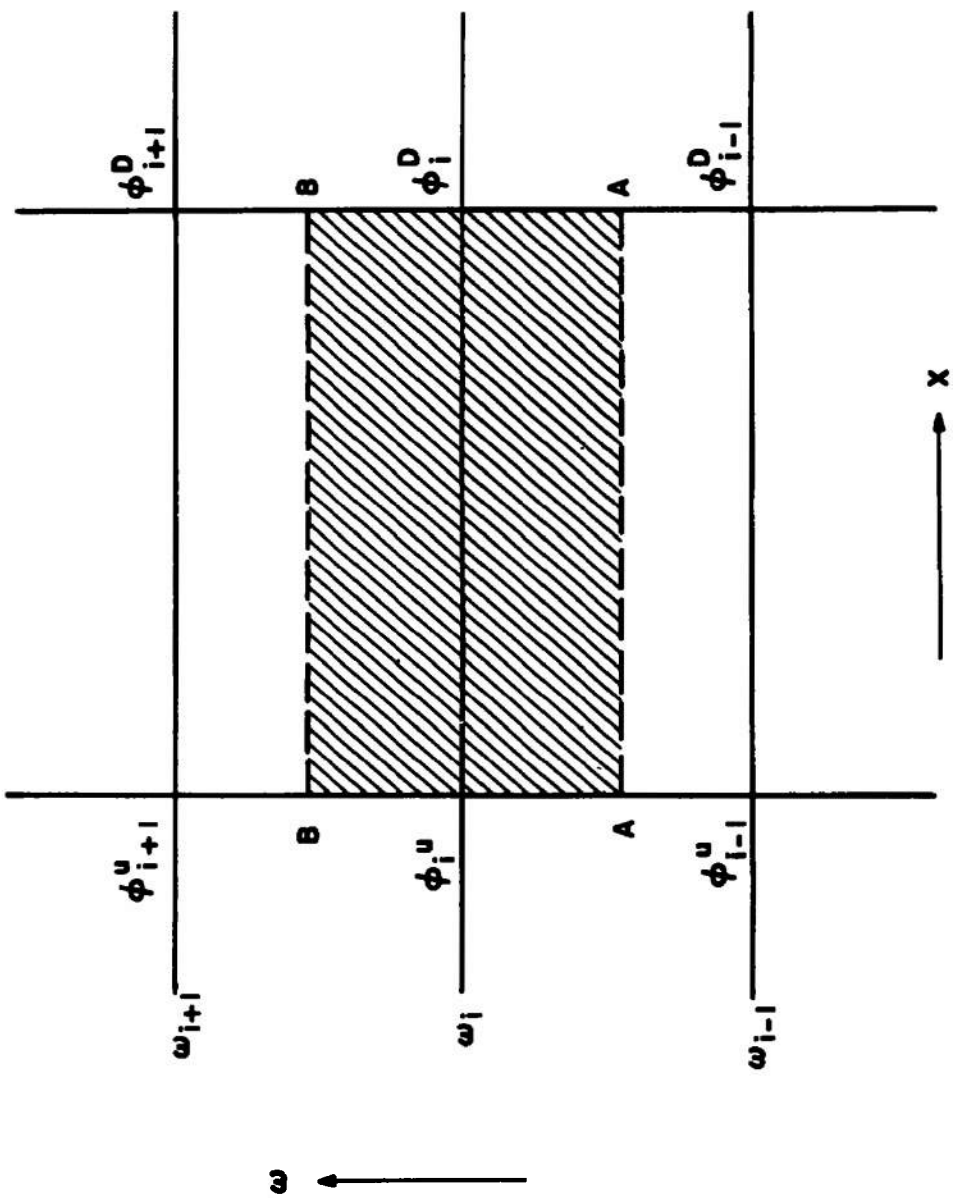

Fig. 2 Control Volume for Linearization of Conservation Equations

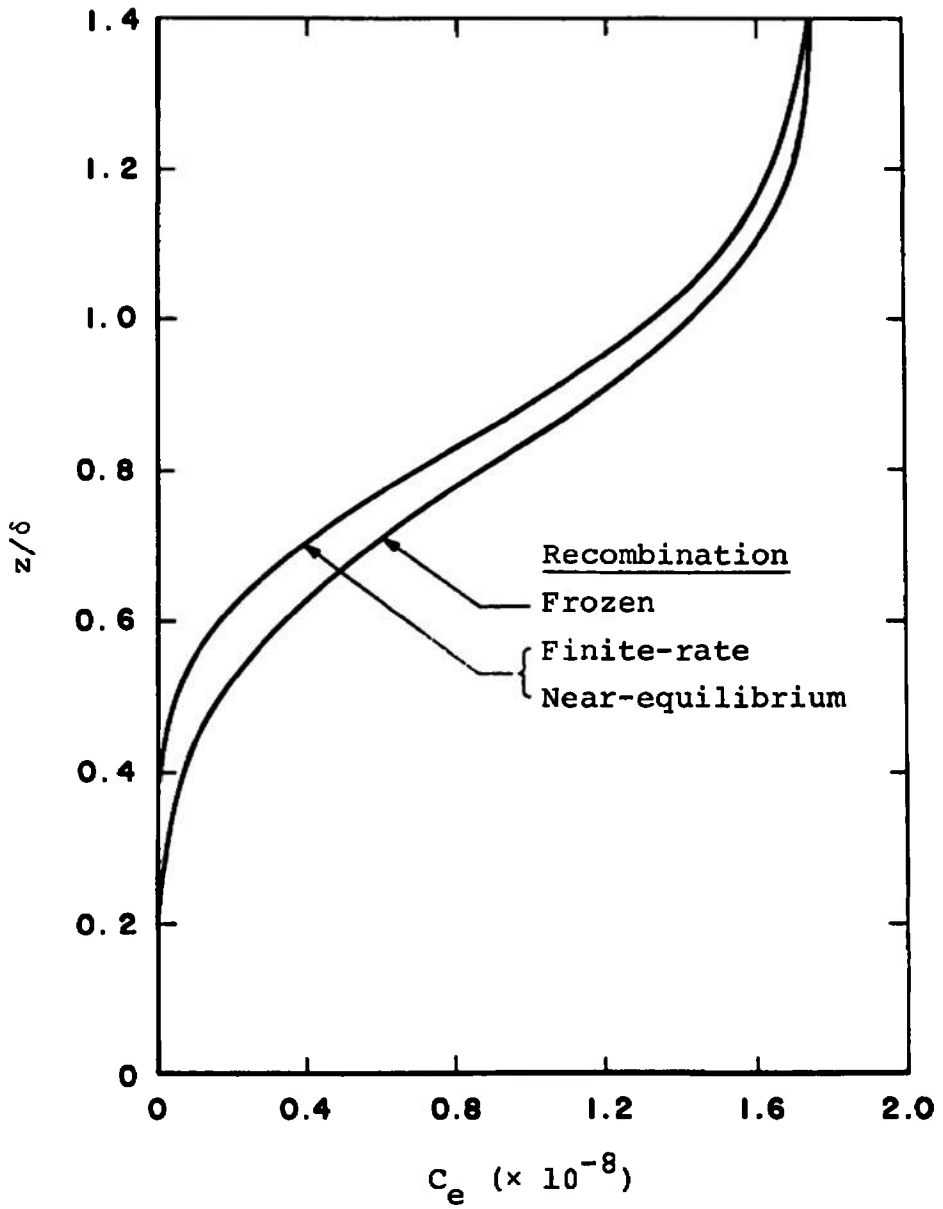

Fig. 3 Non-MHD Initial Electron Concentration Profiles for Different Values of Recombination Rate Coefficient at $x/\ell_o = 0$

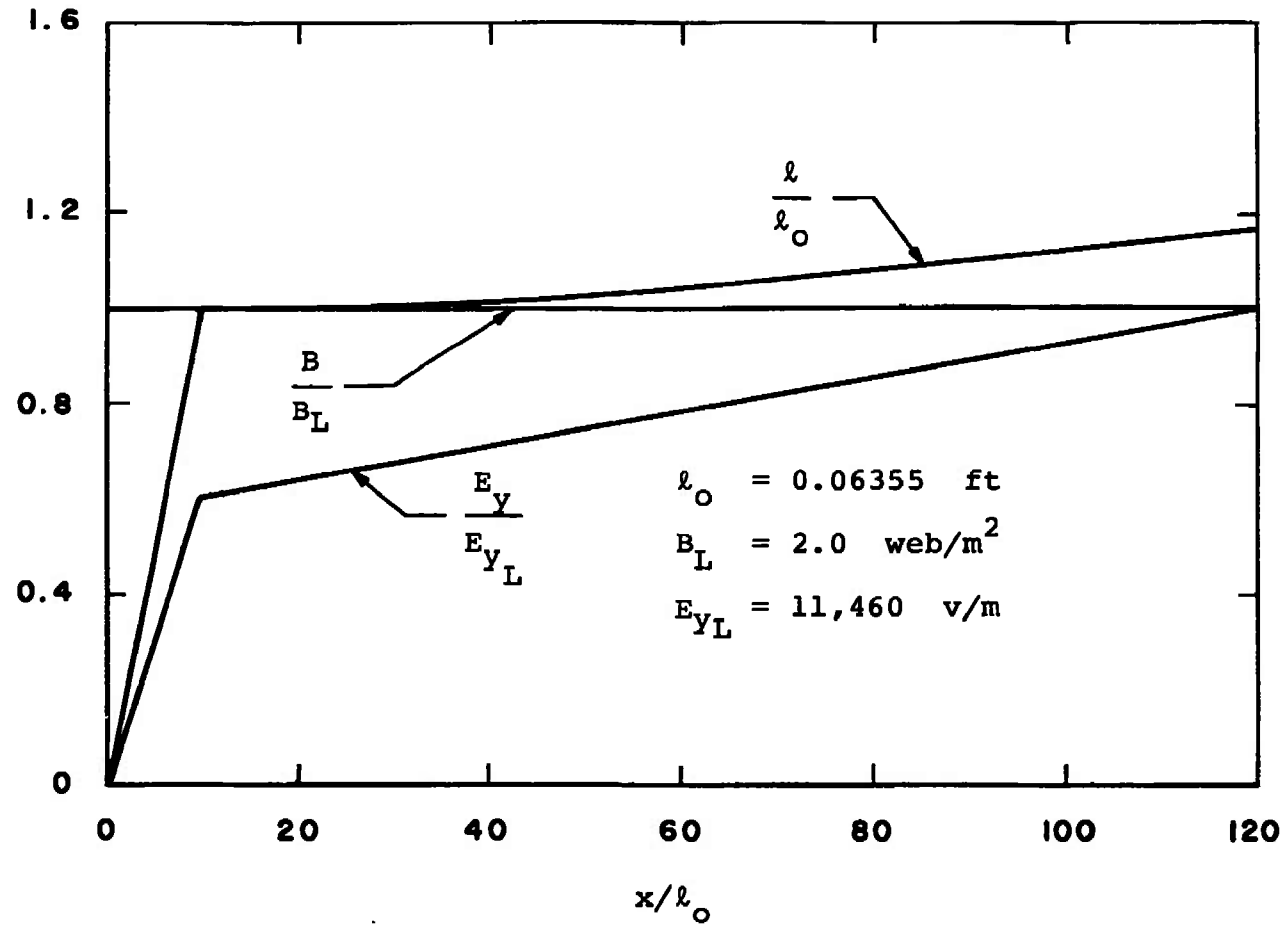

a. Geometry and Field Configuration

Fig. 4 Streamwise Variation of Channel Flow Parameters using Physically Realistic Recombination Rate and Energy-Loss Factor

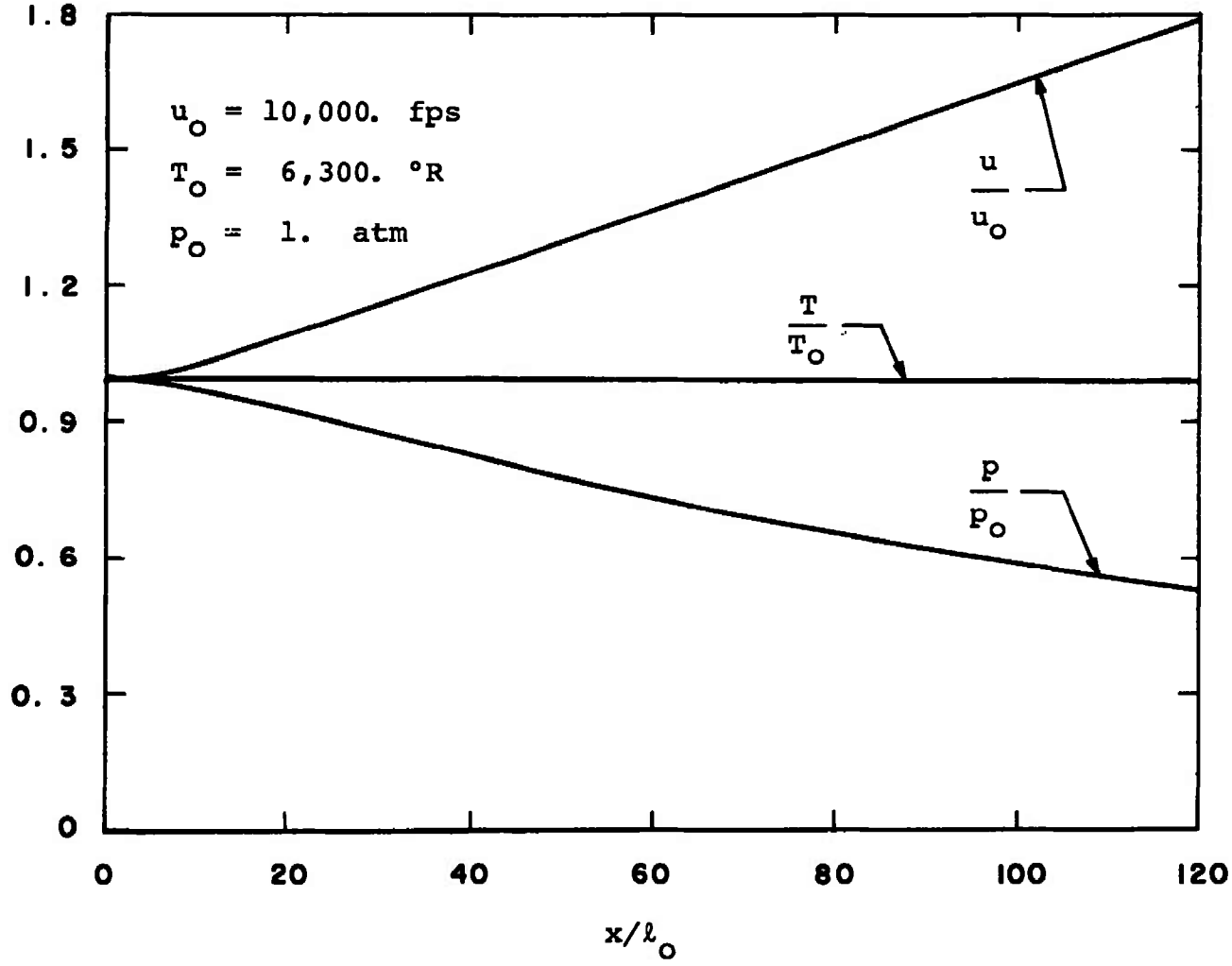

b. Core Flow Properties
Fig. 4 Continued

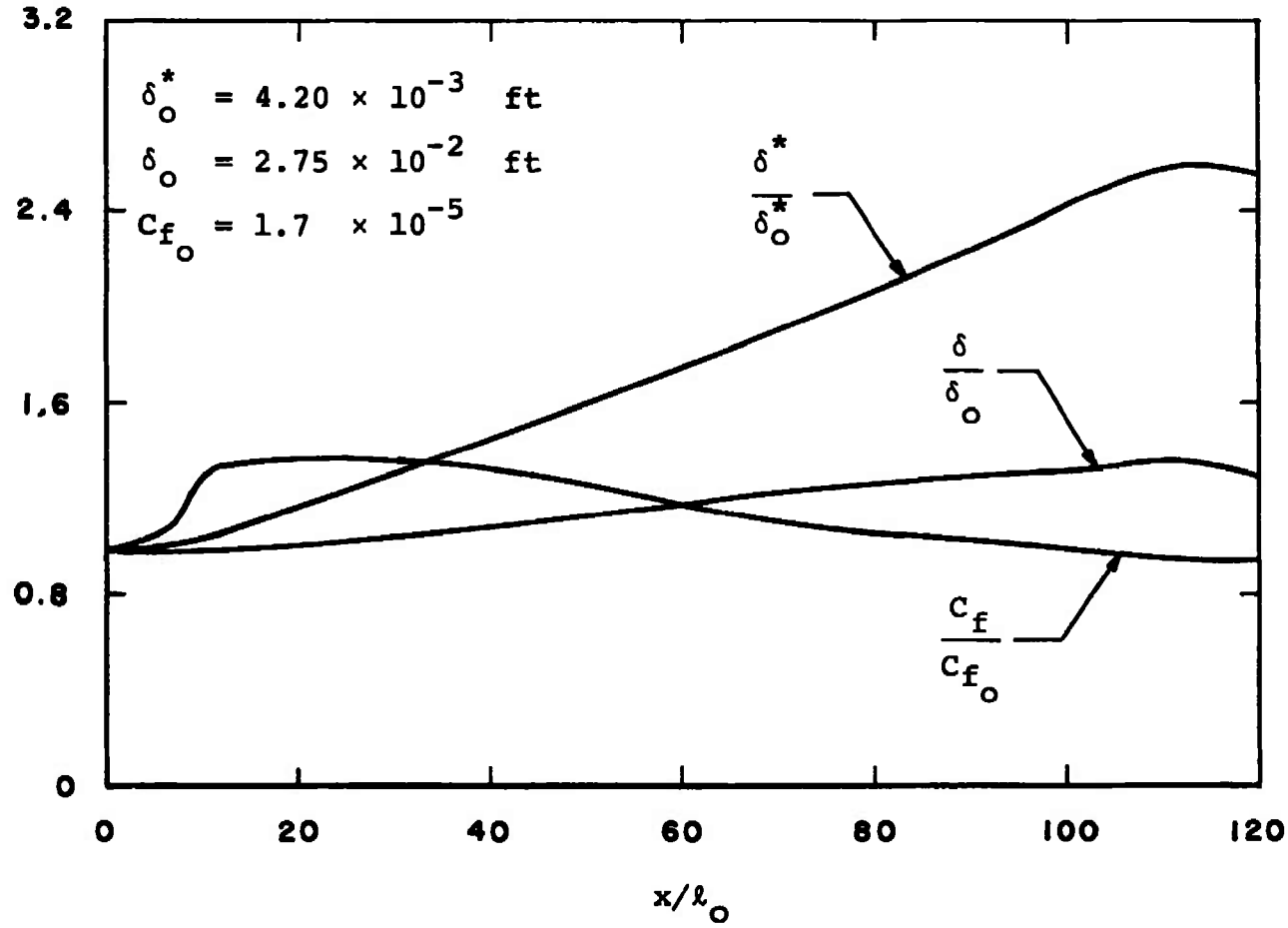

c. Boundary Layer Parameters
Fig. 4 Continued

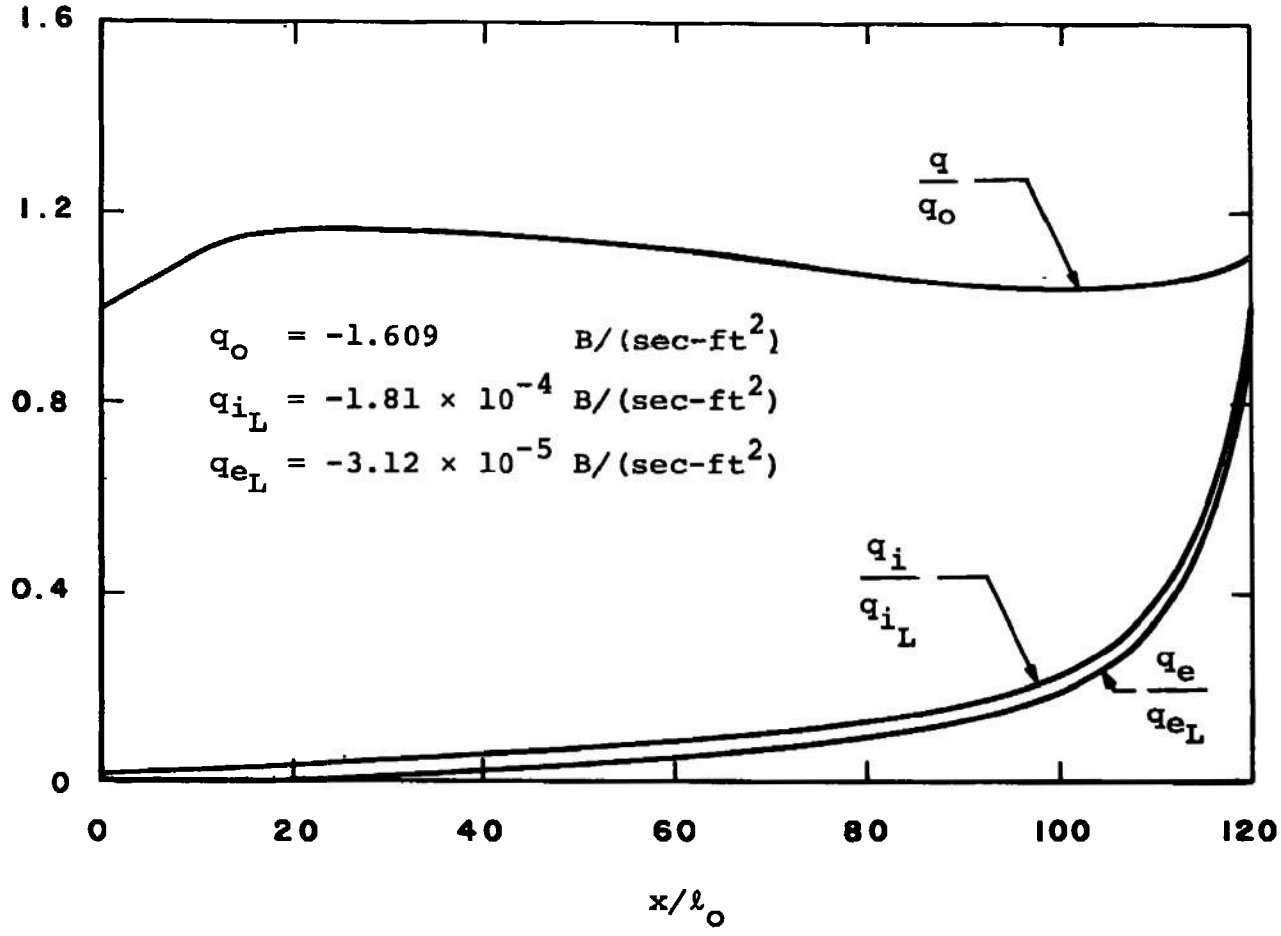

d. Heat Transfer Rates
Fig. 4 Concluded

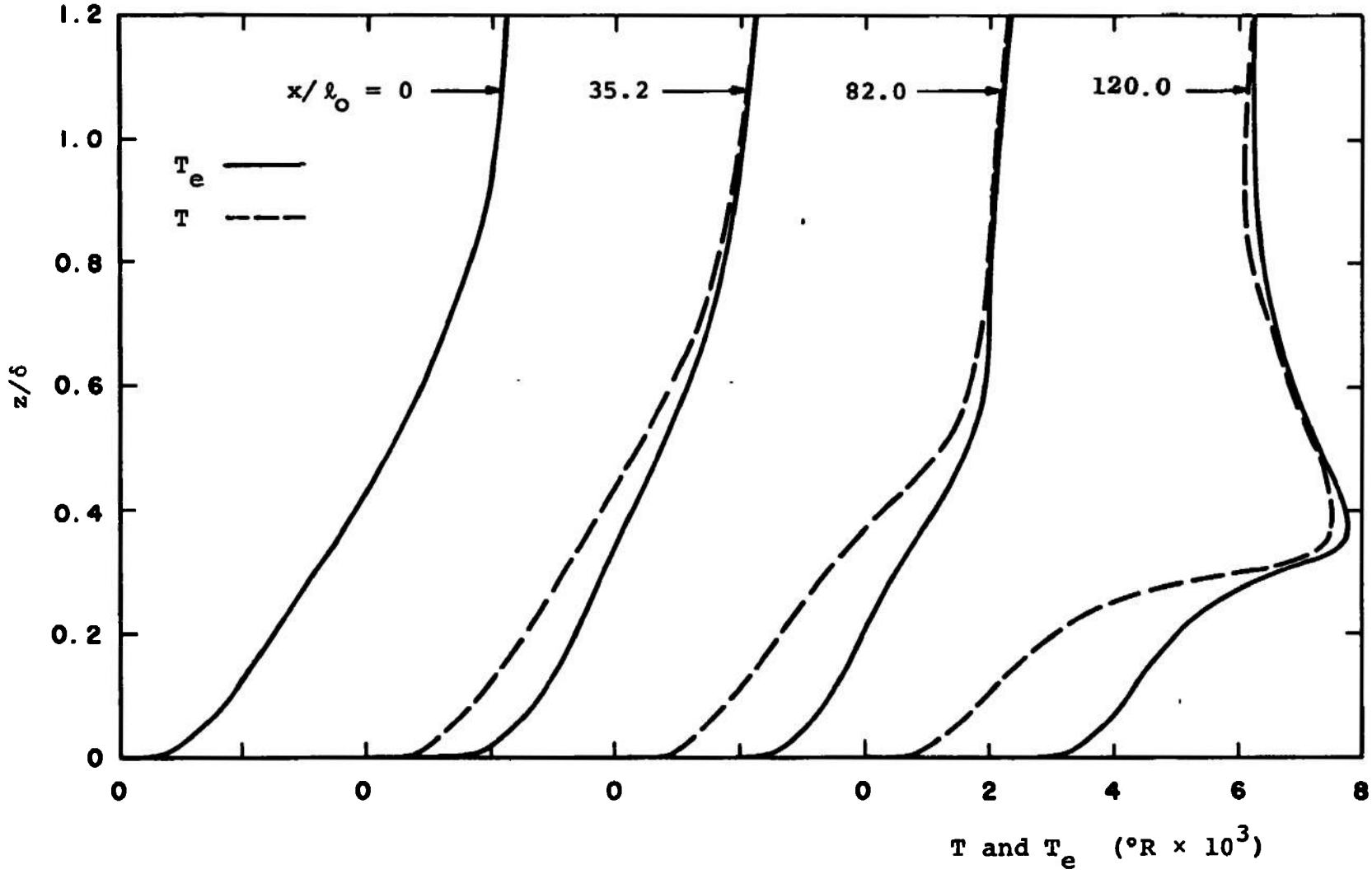

a. Overall and Electron Gas Temperature

Fig. 5 Development of Boundary Layer Profiles using Phsically Realistic Recombination Rate and Energy-Loss Factor

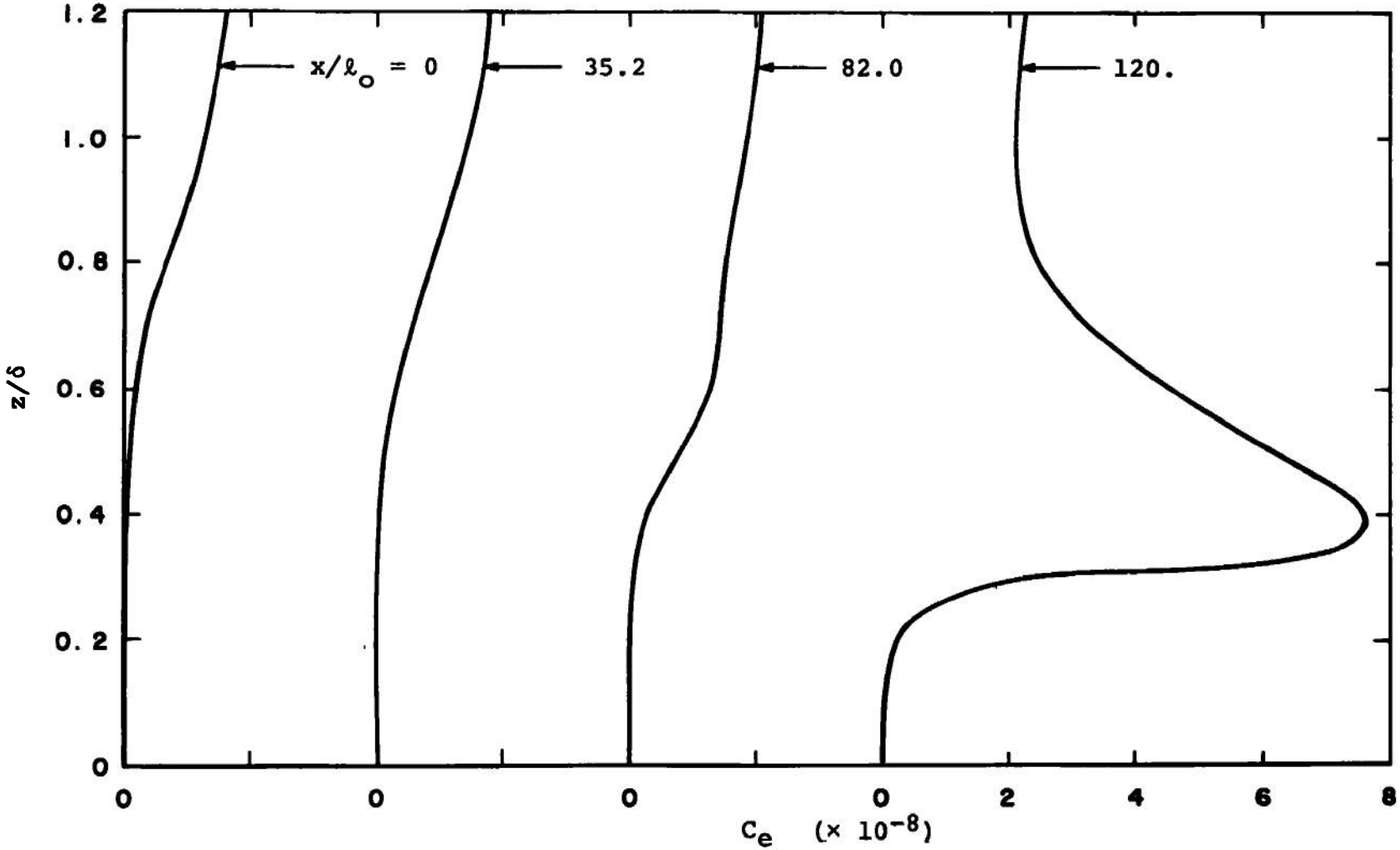

b. Electron Concentration
Fig. 5 Continued

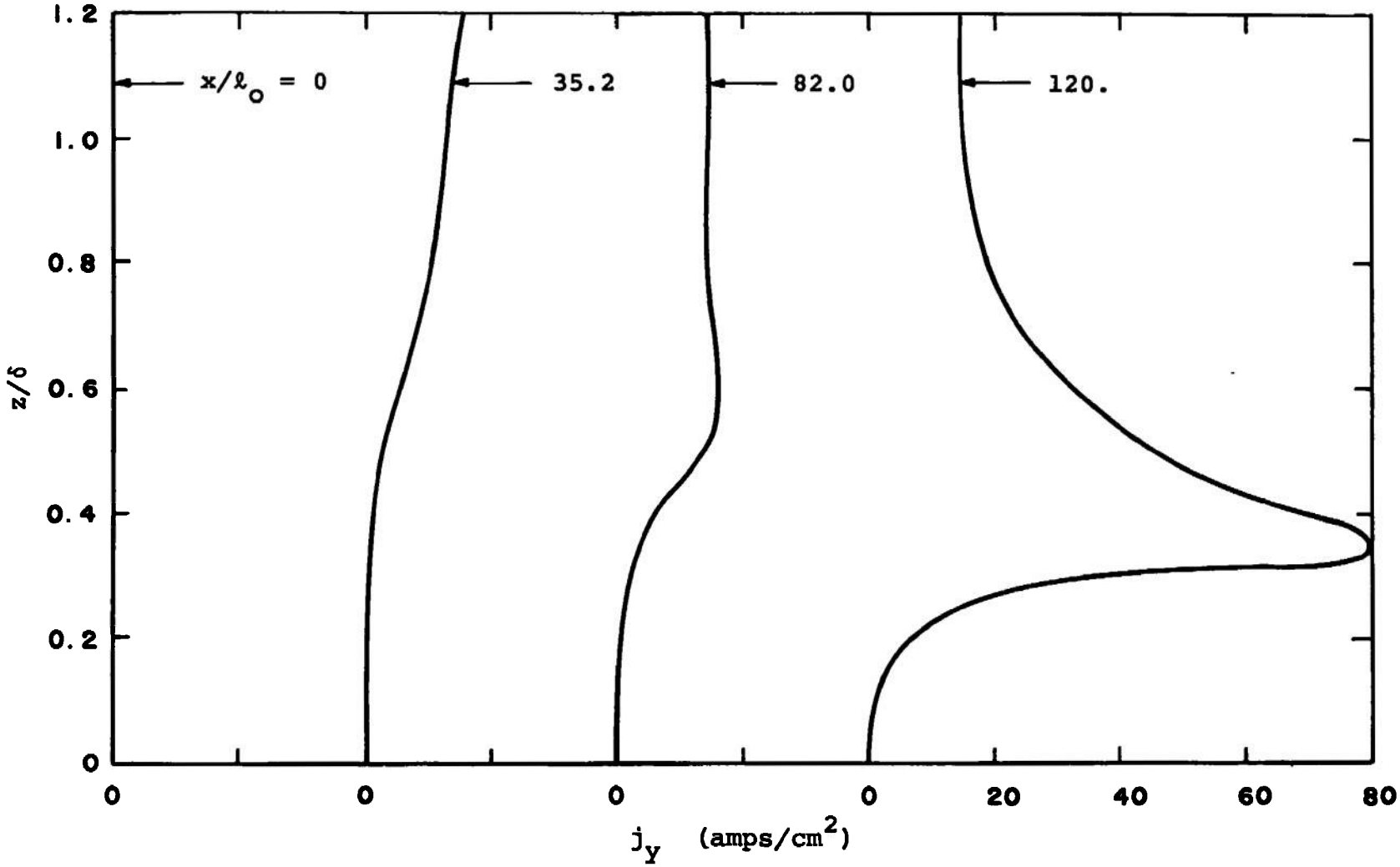

c. Transverse Current Density
Fig. 5 Continued

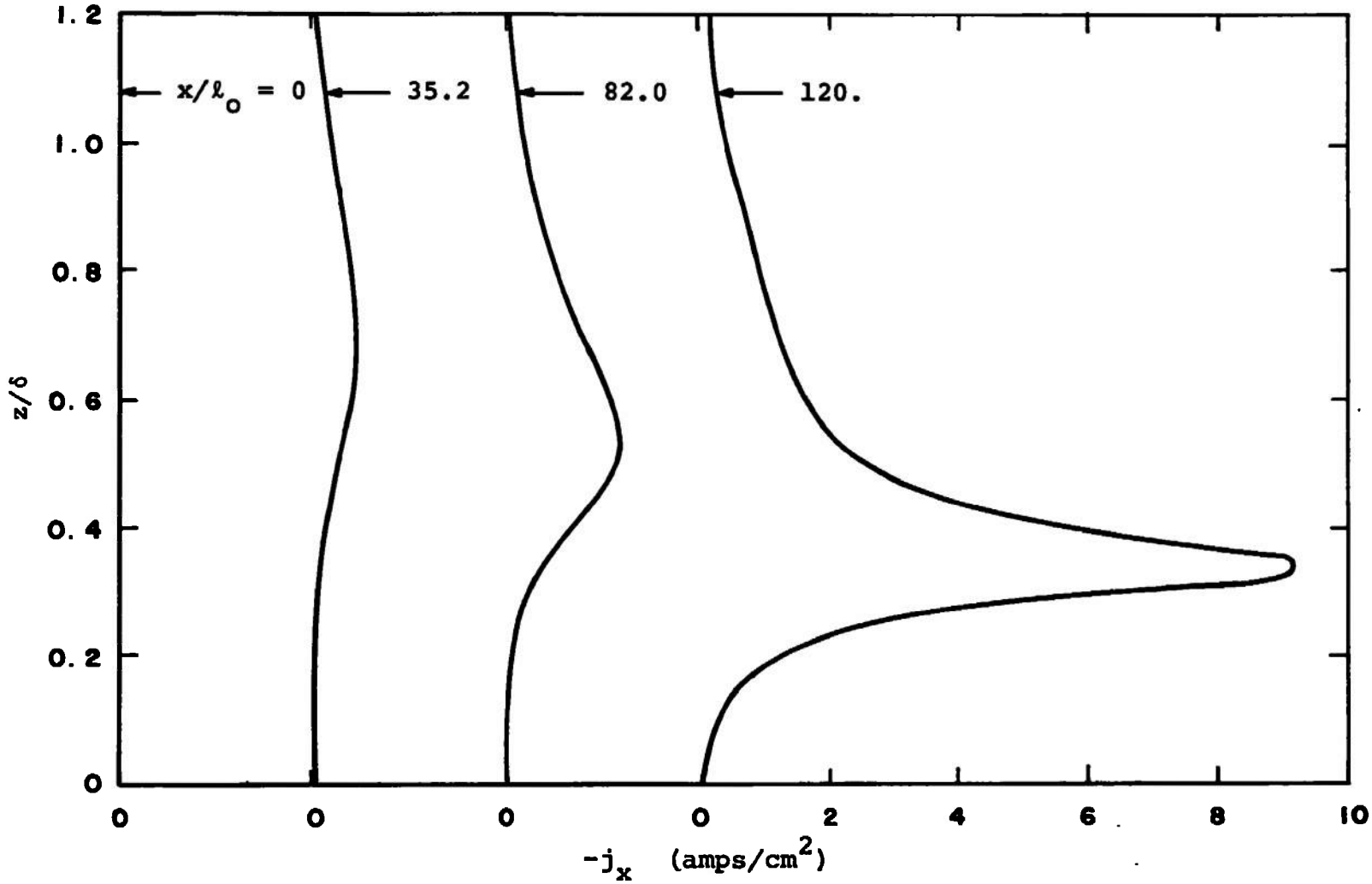

d. Hall Current Density
Fig. 5 Continued

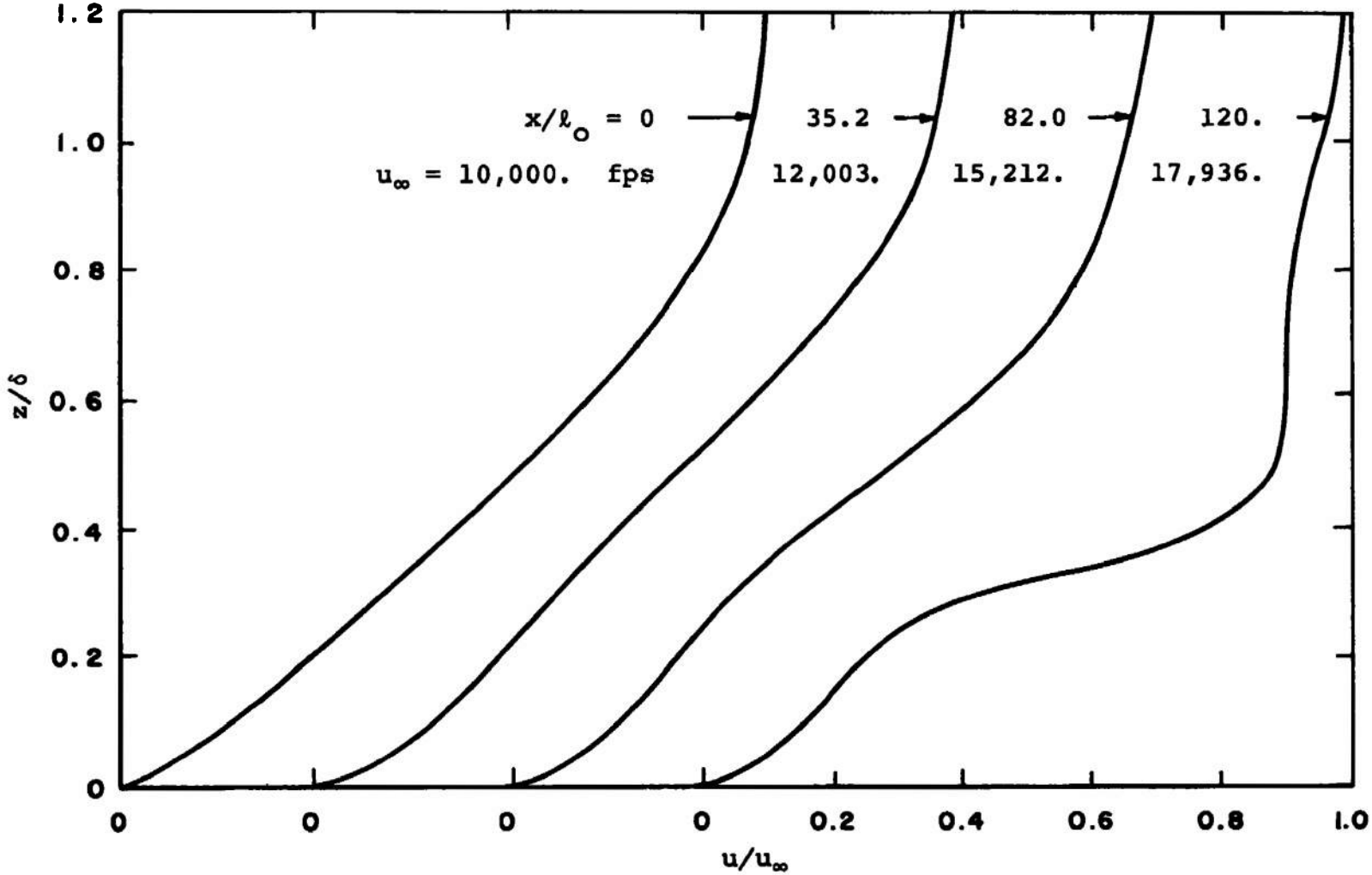

e. Velocity

Fig. 5 Concluded

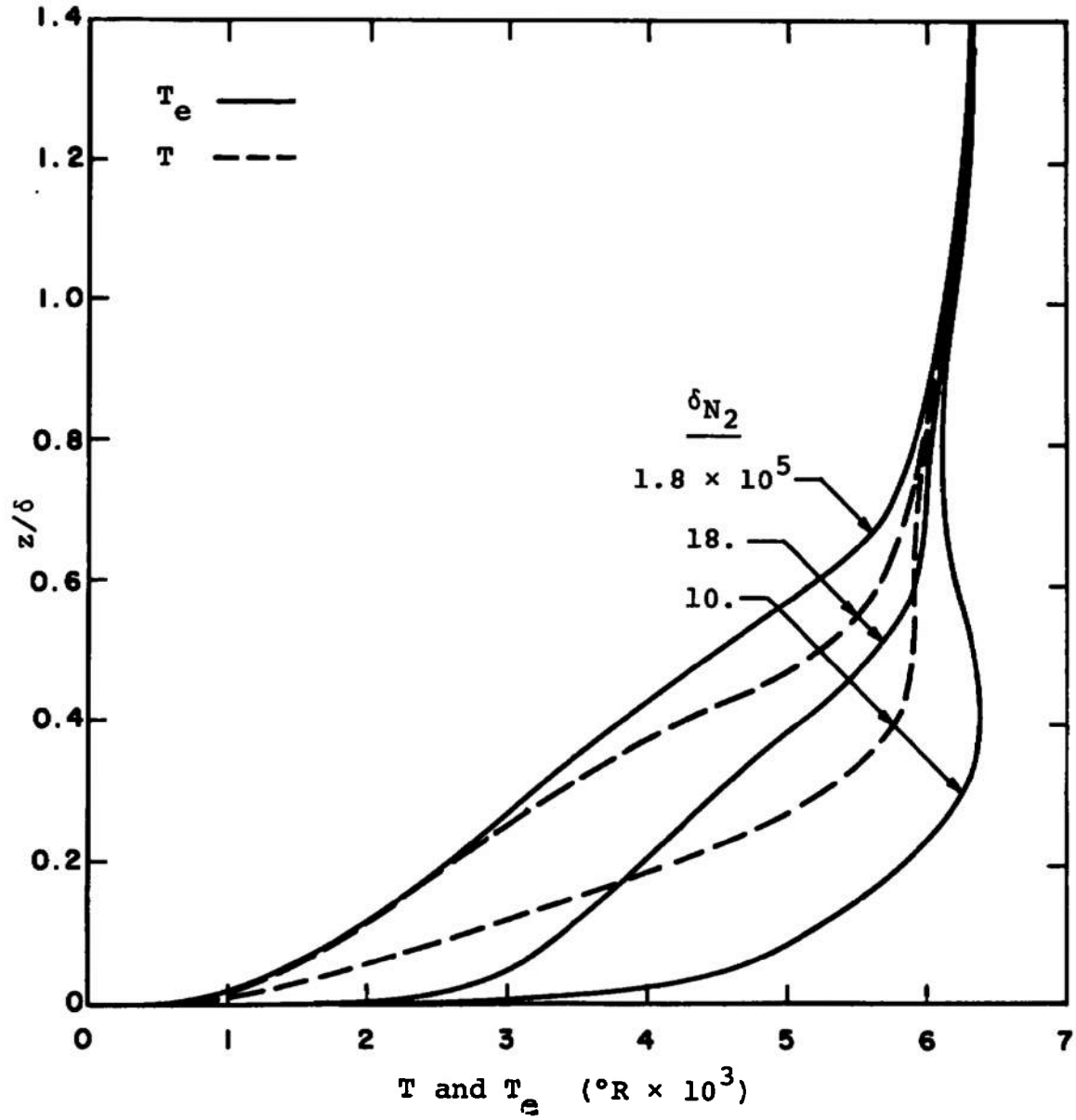

a. Electron and Overall Gas Temperature

Fig. 6 Comparison of Boundary Layer Profiles at x/ℓ_o = 82.0, for Different Values of Energy-Loss Factor

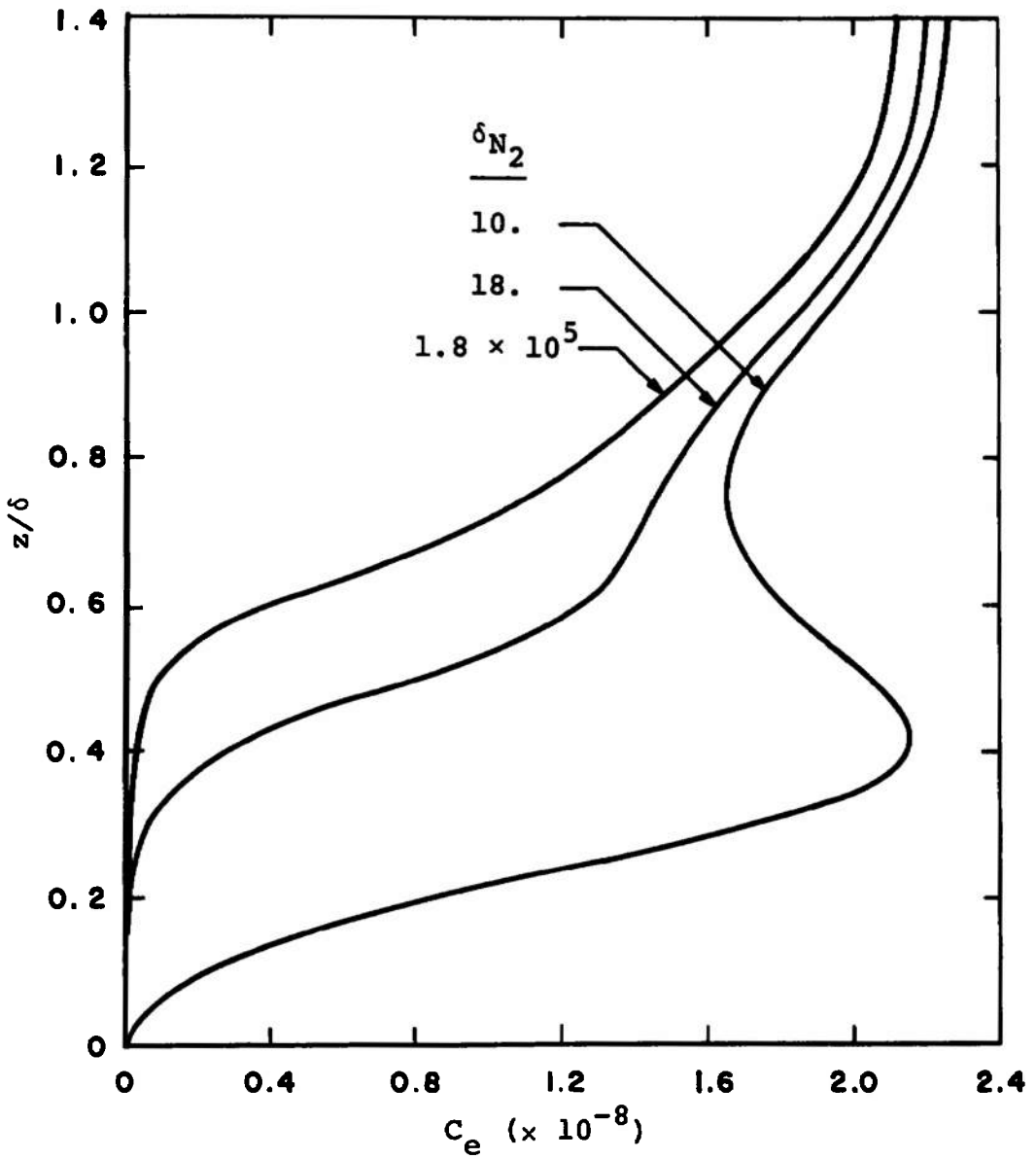

b. Electron Concentration
Fig. 6 Continued

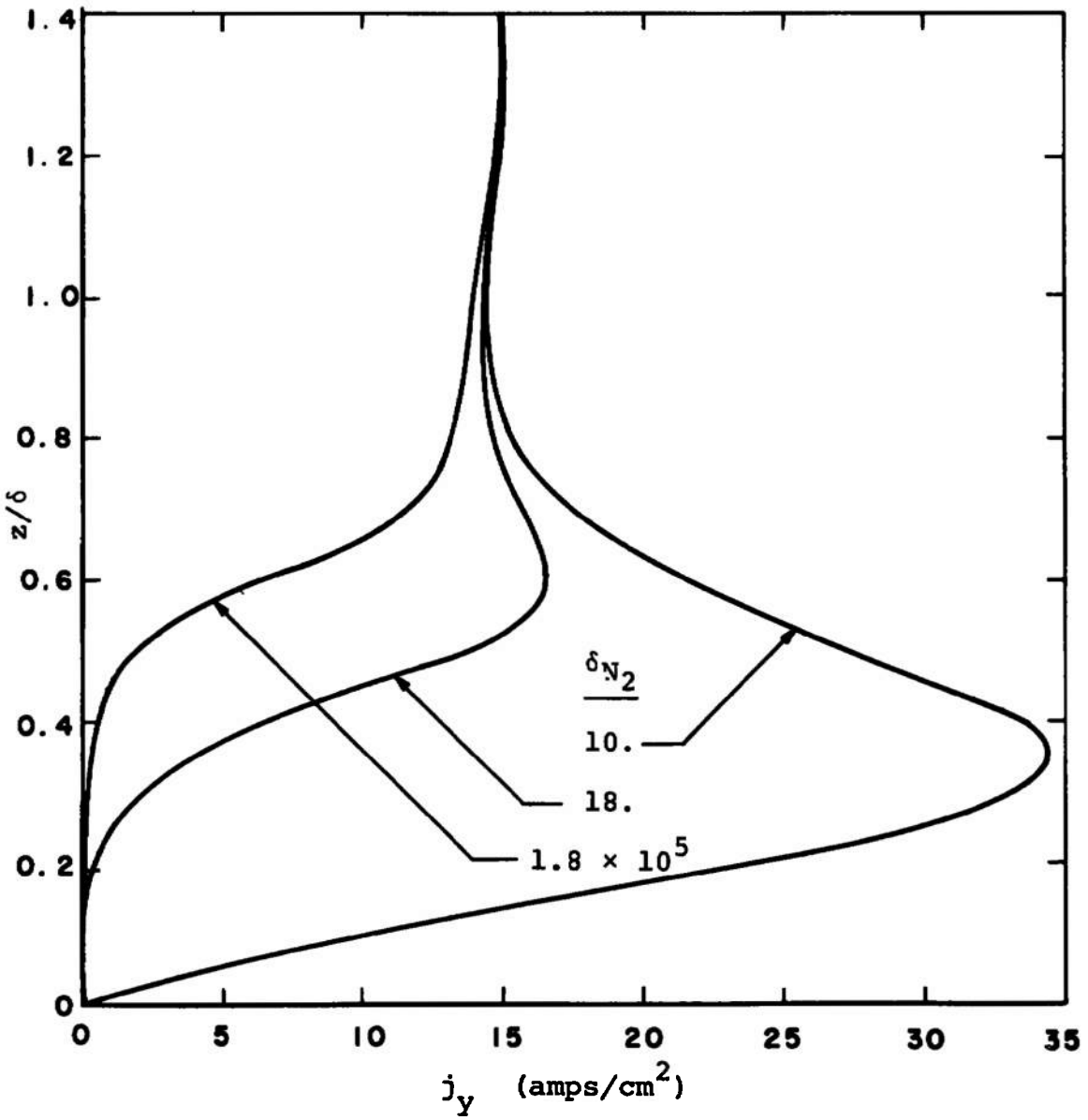

c. Transverse Current
Fig. 6 Concluded

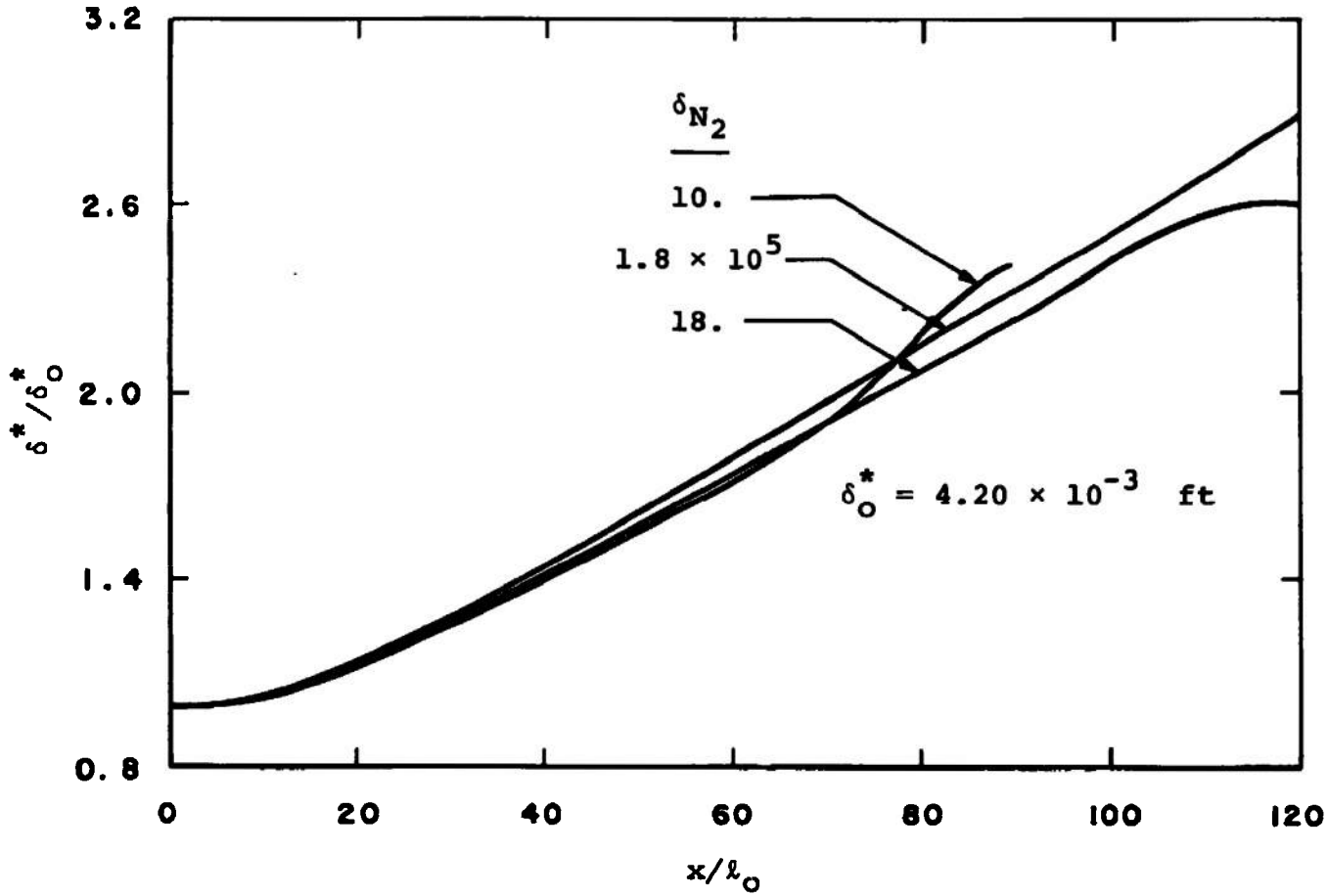

a. Displacement Thickness

Fig. 7 Streamwise Variation of Boundary Layer Parameters for Different Values of Energy-Loss Factor

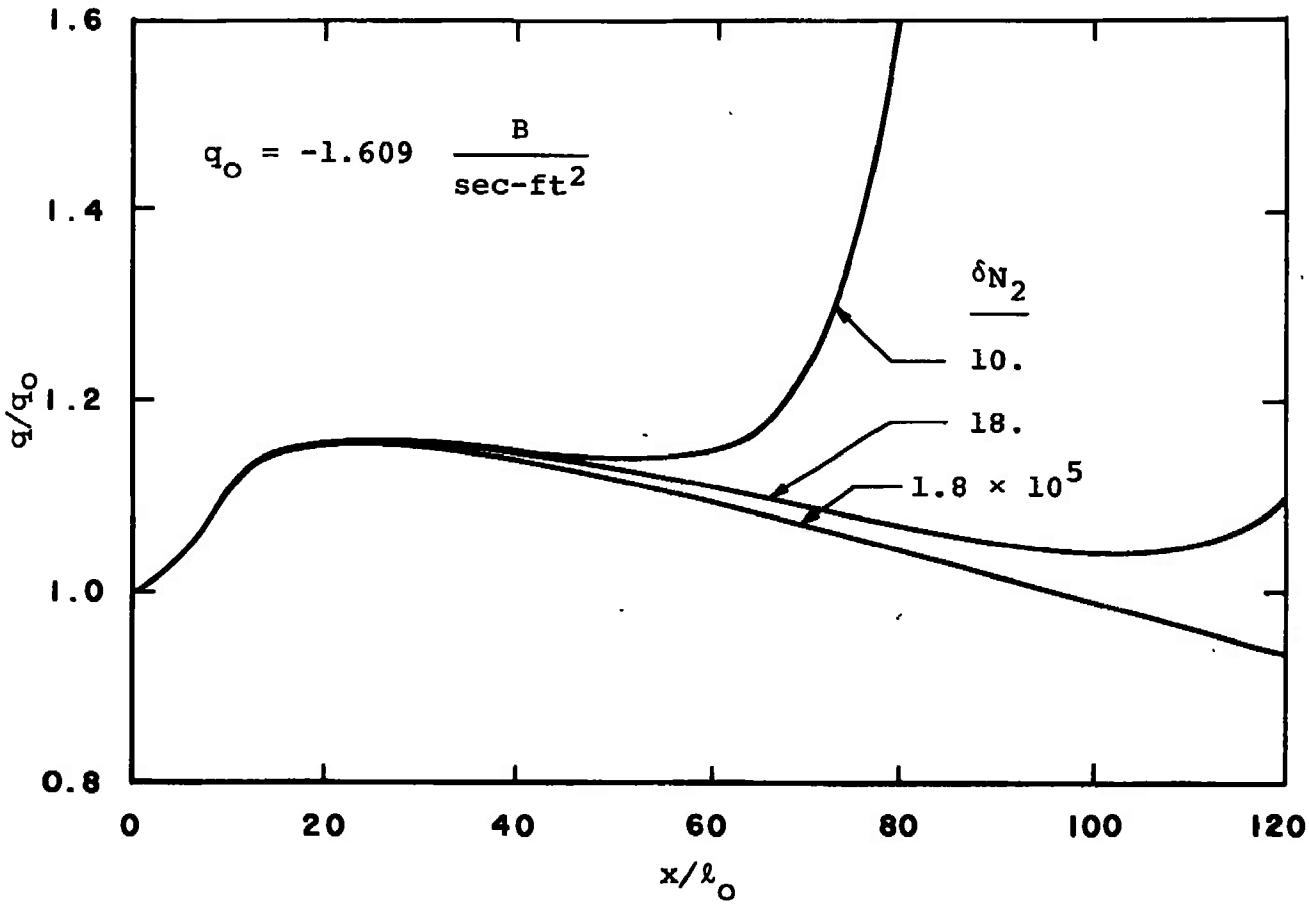

b. Local Heat Flux
Fig. 7 Concluded

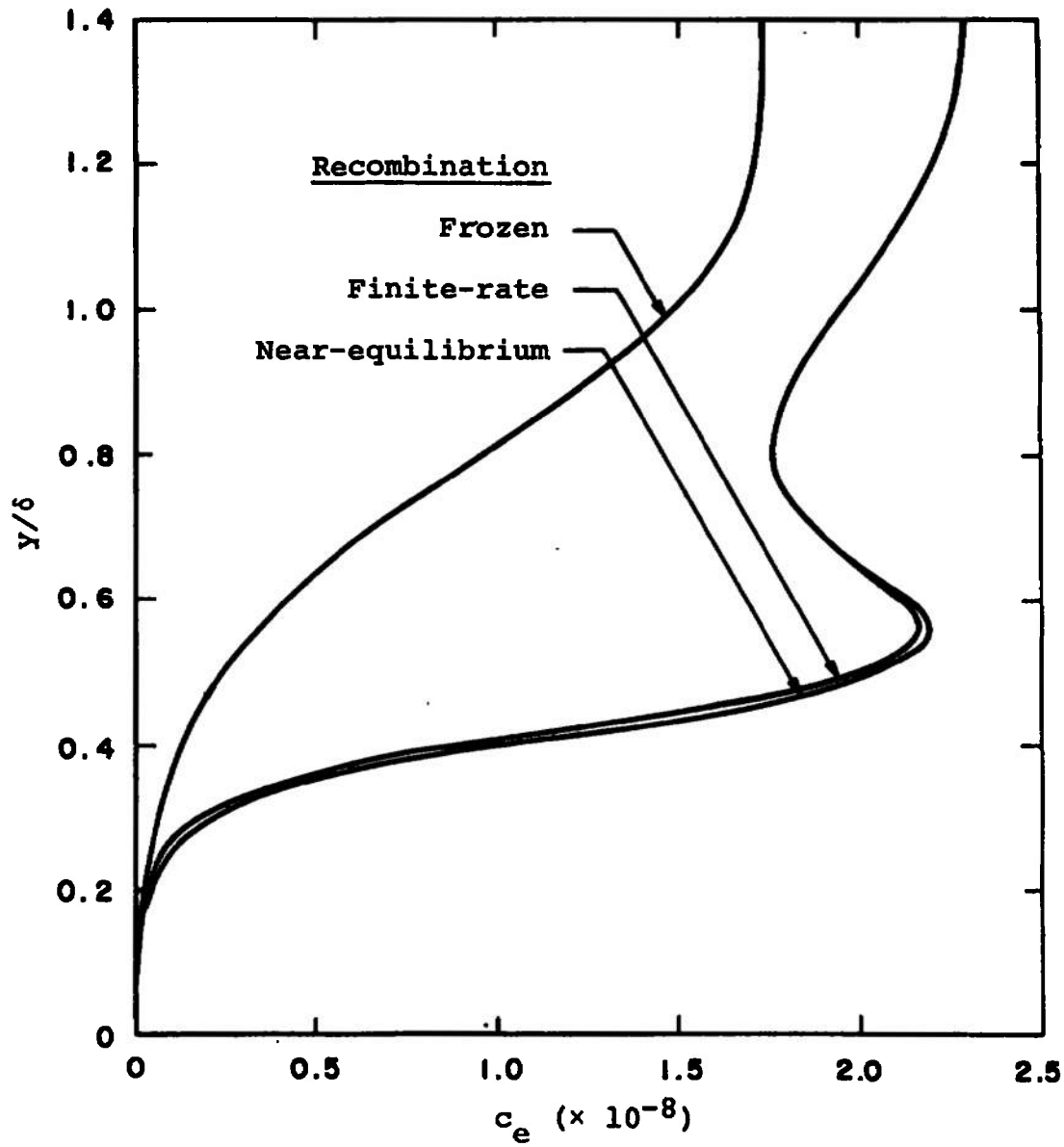

a. Electron Concentration

Fig. 8 Comparison of Boundary Layer Profiles at x/ℓ_o = 96.5 for Different Values of Recombination Rate Coefficient

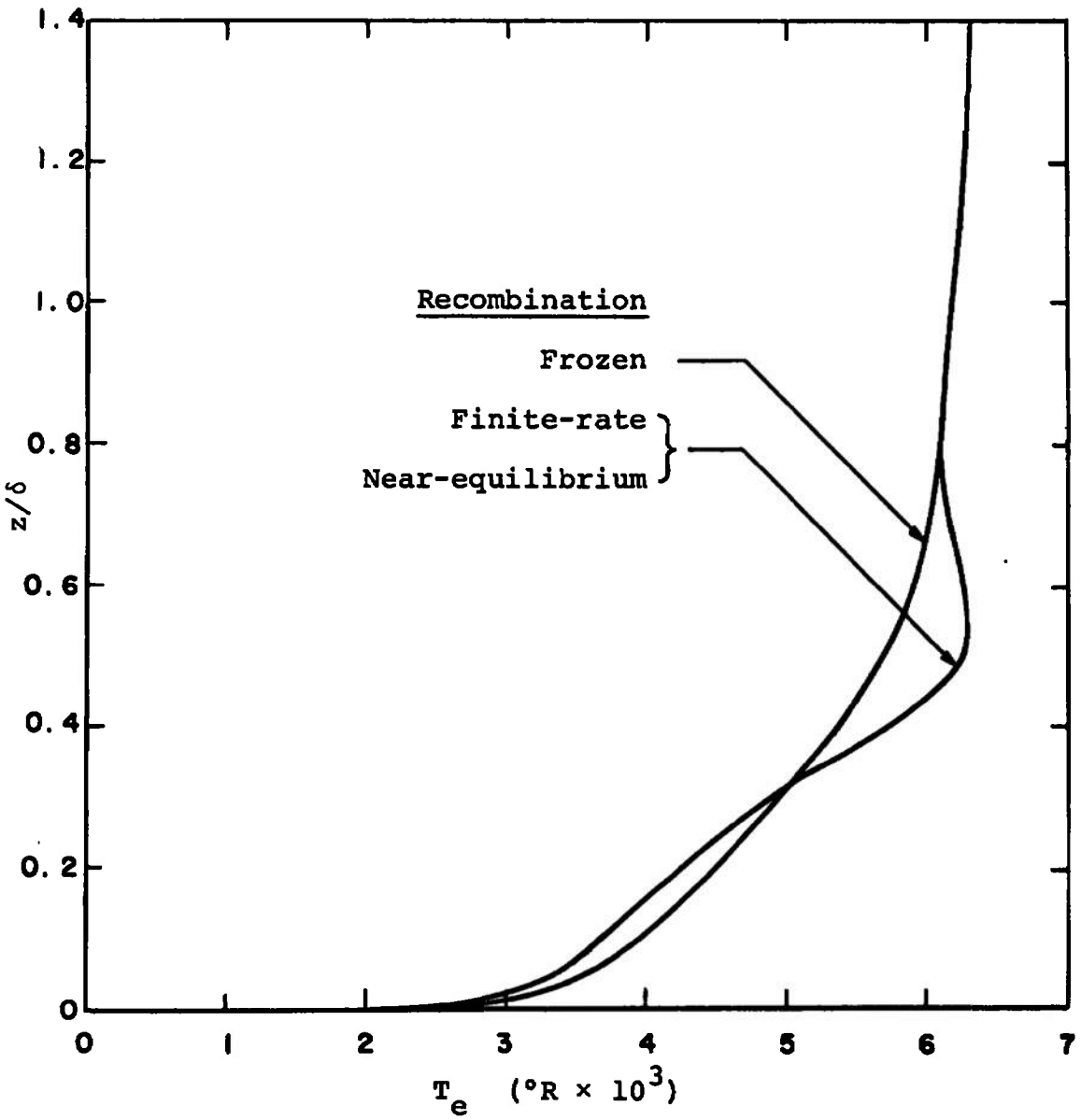

b. Electron Temperature
Fig. 8 Continued

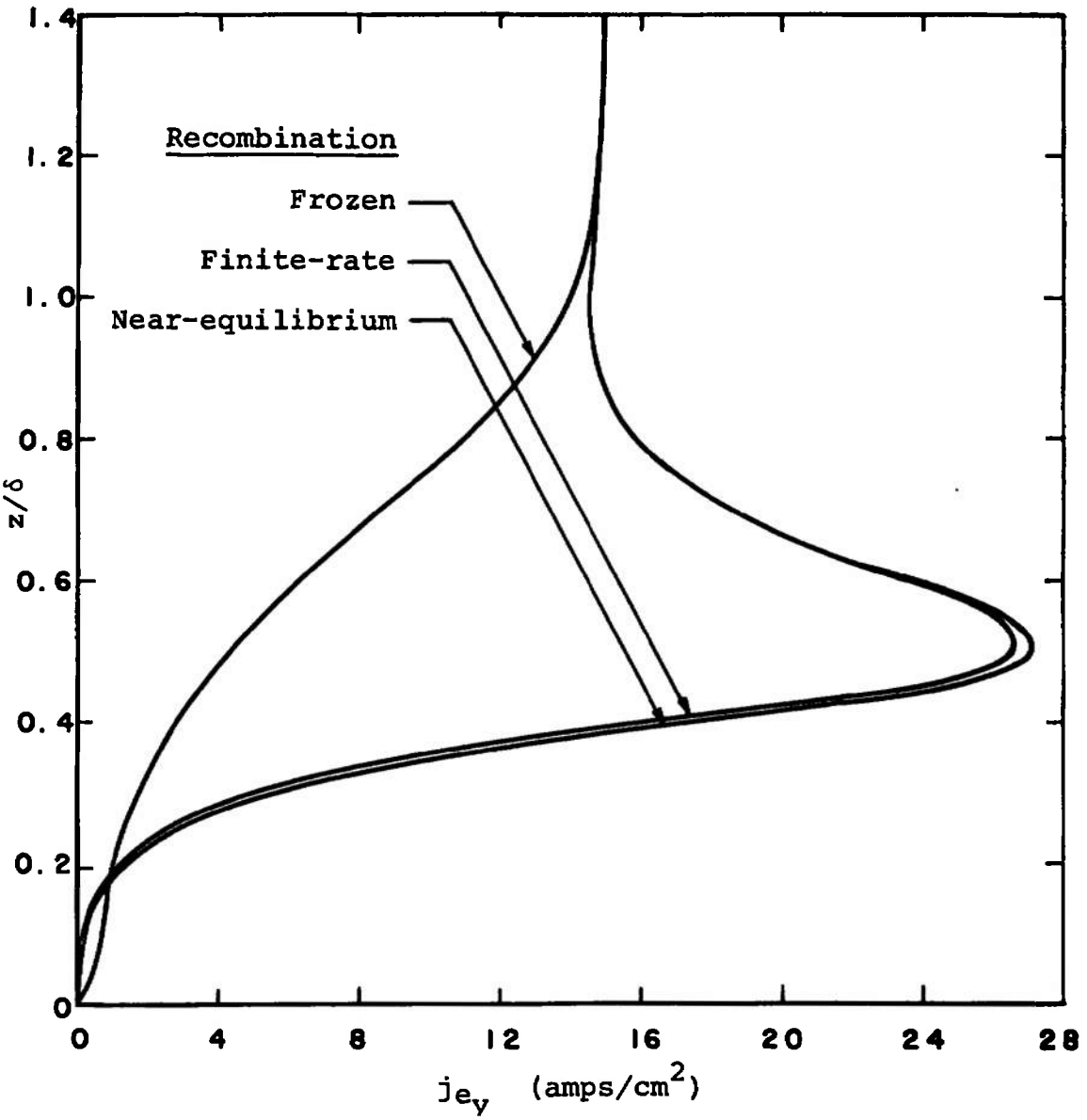

c. Transverse Current Density
Fig. 8 Concluded

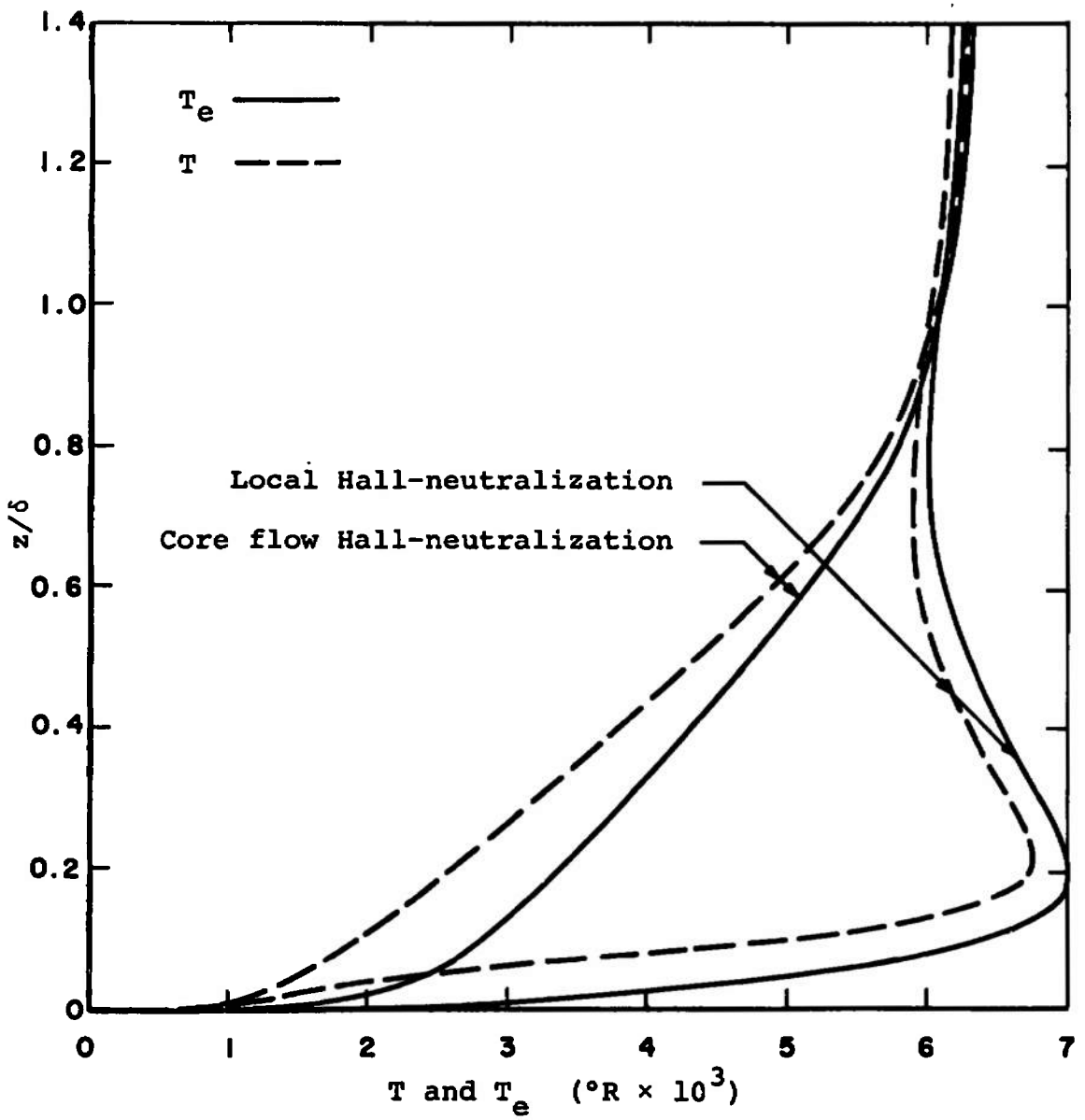

a. Electron and Overall Gas Temperatures

Fig. 9 Comparison of Boundary Layer Profiles for Core Flow and Local Hall-Neutralization at $x/\ell_0 = 35.2$

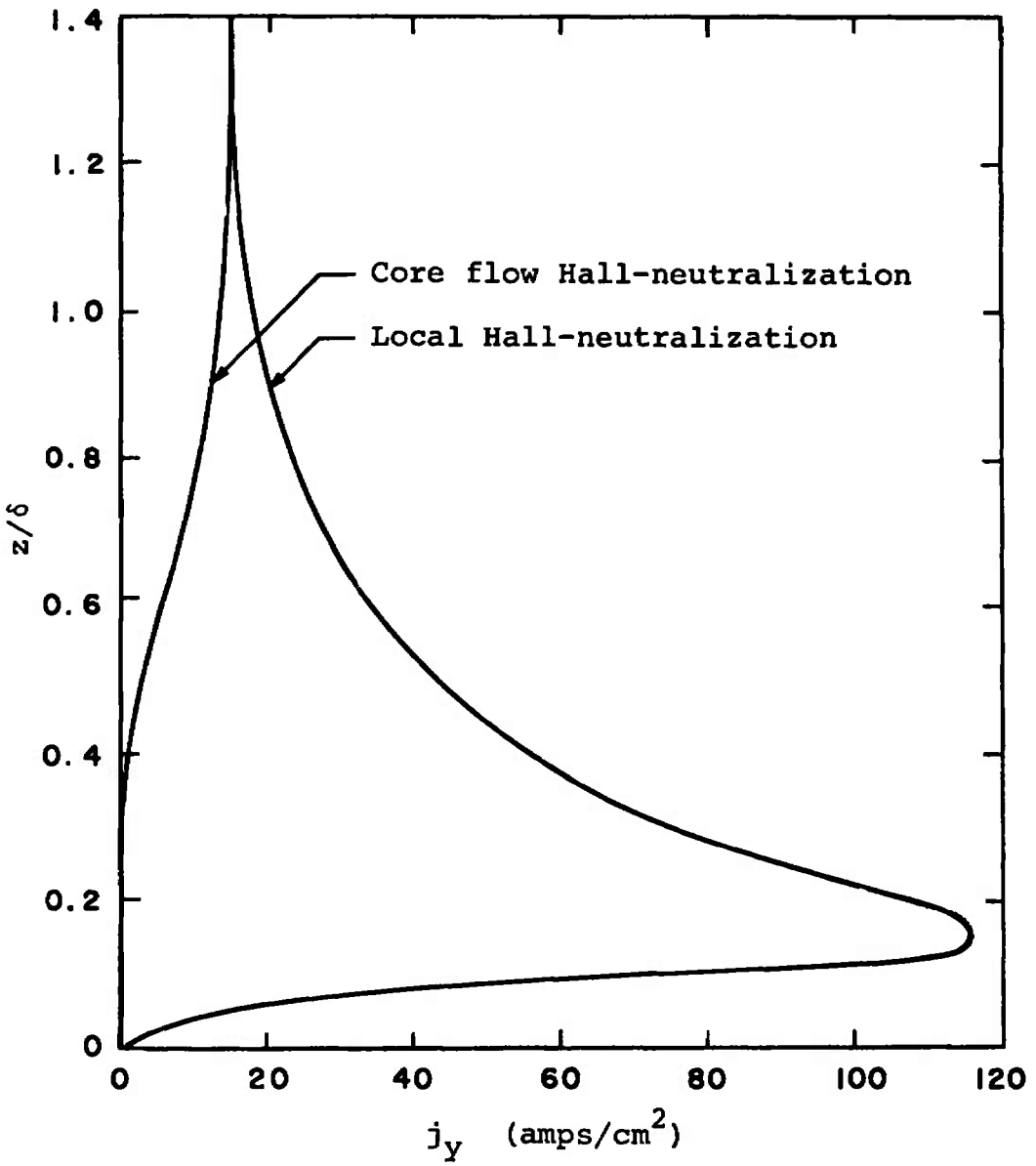

b. Trasverse Current Density
Fig. 9 Continued

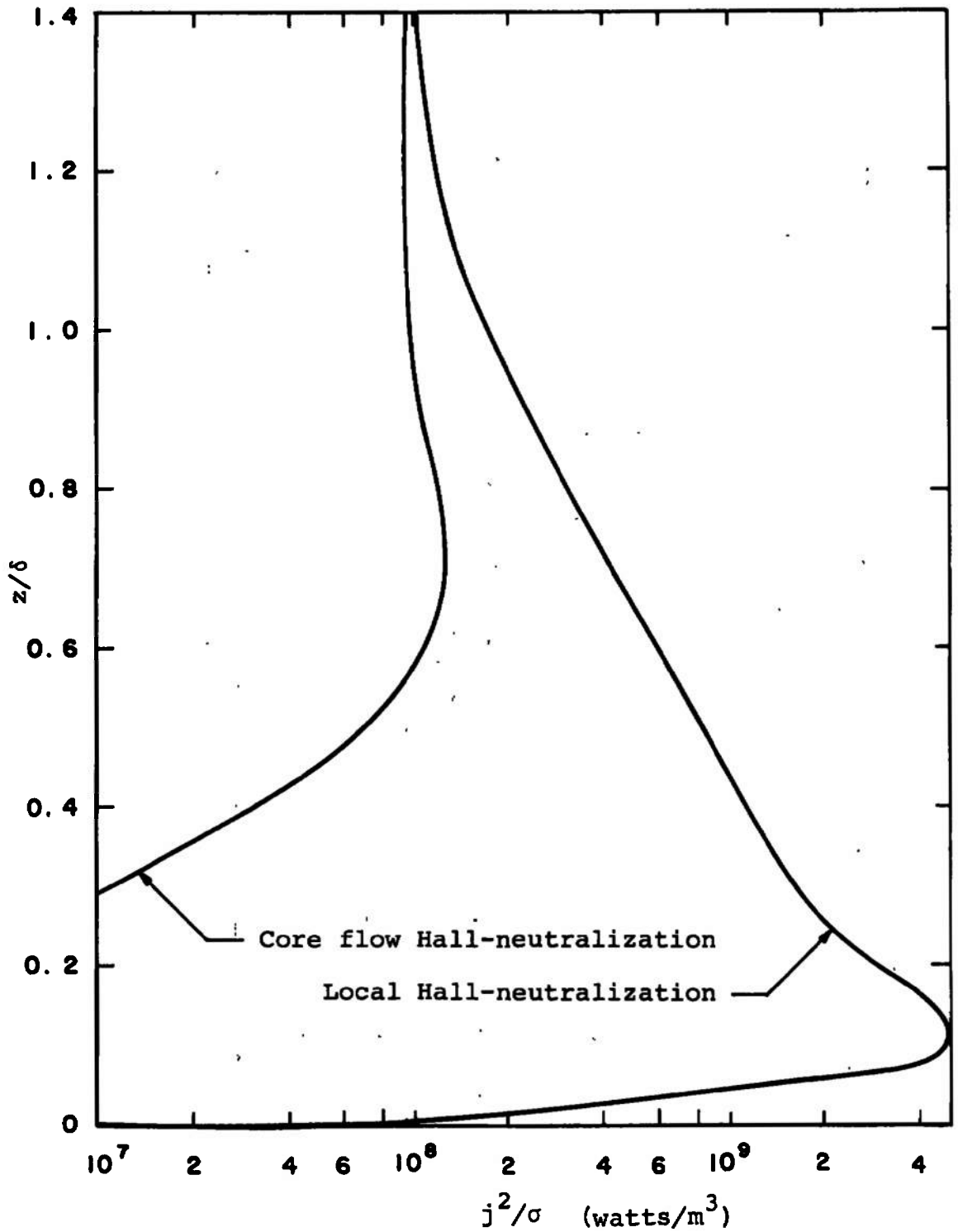

c. Joule Dissipation

Fig. 9 Concluded

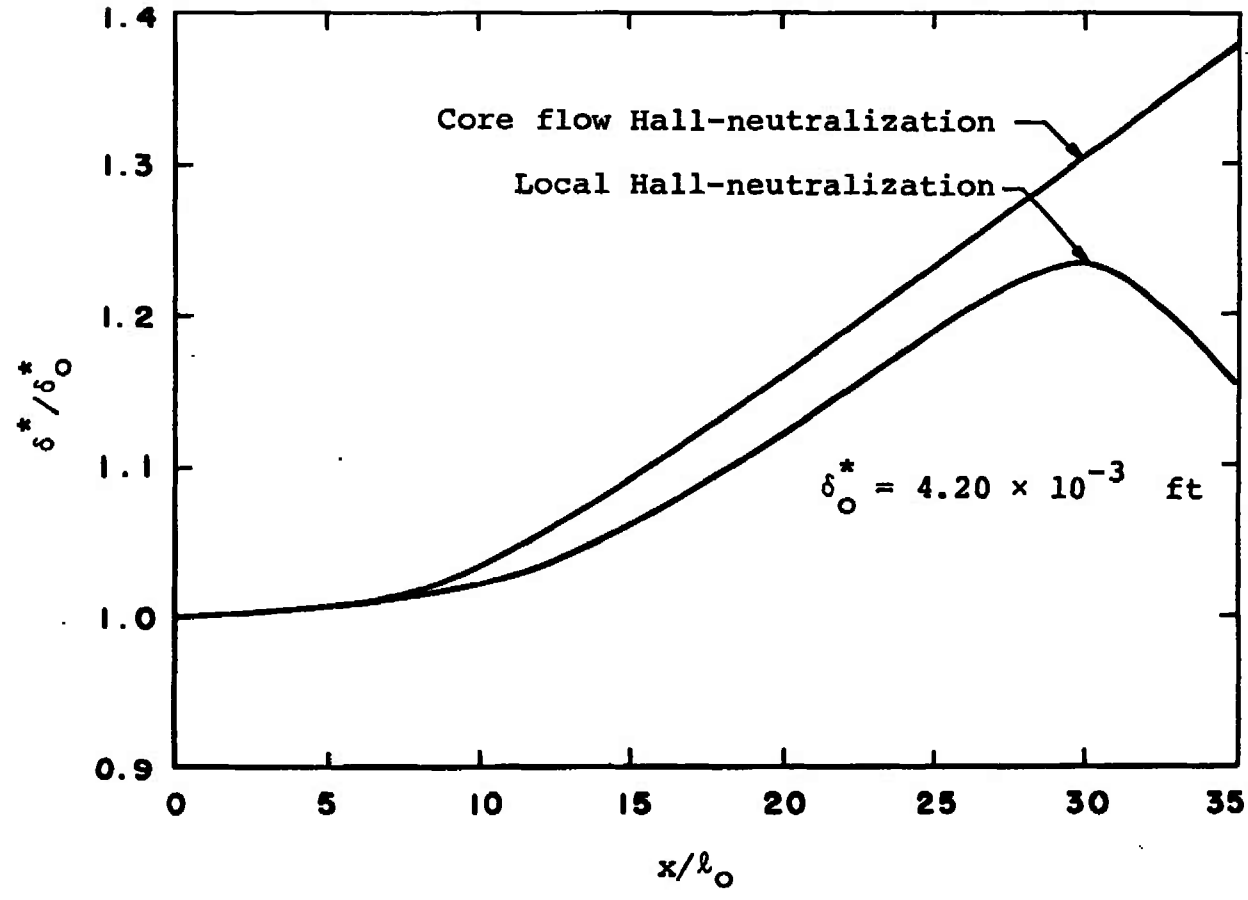

a. Displacement Thickness

Fig. 10 Streamwise Variation of Boundary Layer Parameters for Local and Core Flow Hall-Neutralization

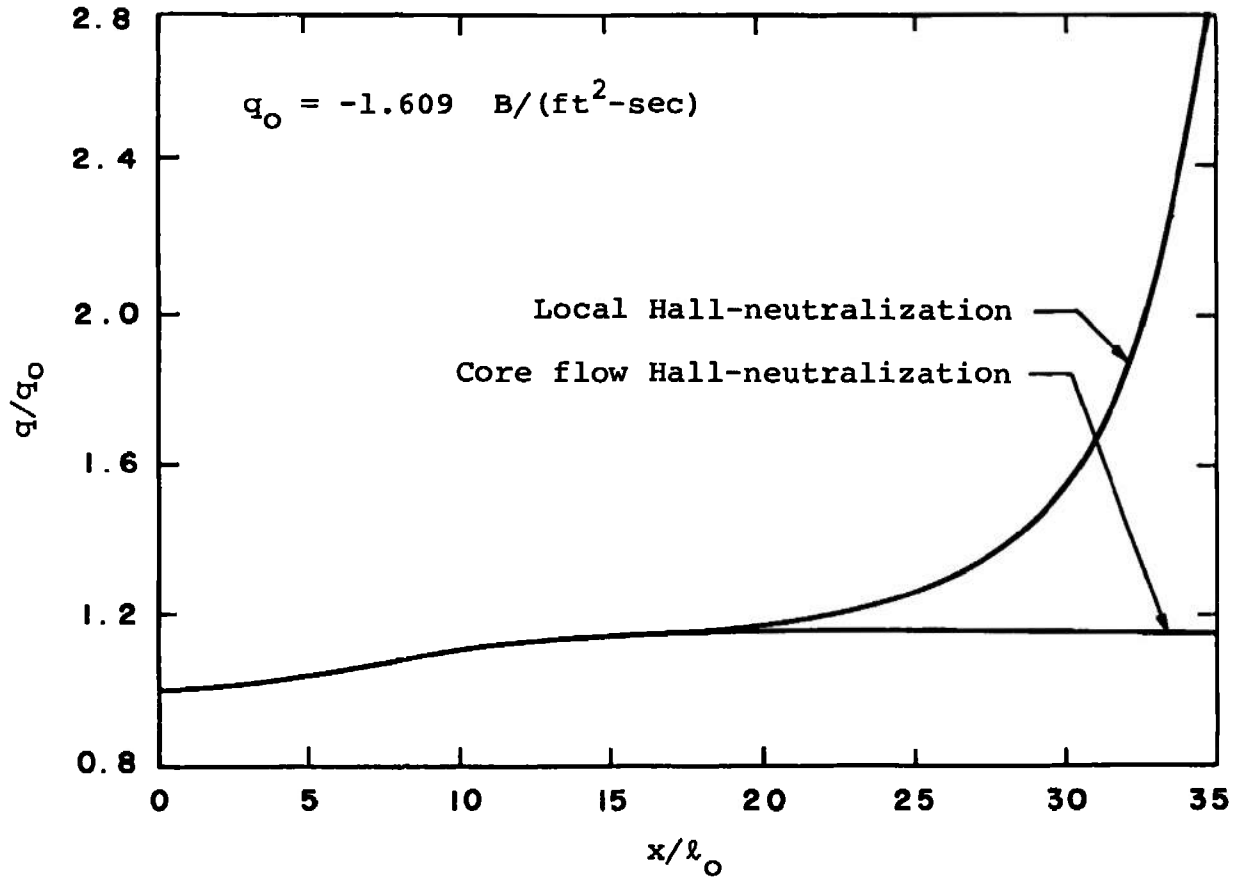

b. Local Heat Transfer
Fig. 10 Concluded

UNCLASSIFIED

Security Classification

DOCUMENT CONTROL DATA - R & D

(Security classification of title, body of abstract and indexing annotation must be entered when the overall report is classified)

1. ORIGINATING ACTIVITY (Corporate author)	2a. REPORT SECURITY CLASSIFICATION
Arnold Engineering Development Center, ARO, Inc., Operating Contractor, Arnold Air Force Station, Tennessee 37389	UNCLASSIFIED
	2b. GROUP N/A

3. REPORT TITLE

IONIZATIONAL AND THERMAL NONEQUILIBRIUM IN MHD BOUNDARY LAYERS

4. DESCRIPTIVE NOTES (Type of report and inclusive dates)

July 1, 1968 to June 30, 1969 - Final Report

5. AUTHOR(S) (First name, middle initial, last name)

Donald W. Cott, ARO, Inc.

6. REPORT DATE	7a. TOTAL NO. OF PAGES	7b. NO. OF REFS
November 1970	68	16

8a. CONTRACT OR GRANT NO	9a. ORIGINATOR'S REPORT NUMBER(S)
F40600-71-C-0002	
b. Program Element 64719F	AEDC-TR-70-231
c.	9b. OTHER REPORT NO(S) (Any other numbers that may be assigned this report)
d.	ARO-PWT-TR-70-155

10. DISTRIBUTION STATEMENT

This document has been approved for public release and sale; its distribution is unlimited.

11. SUPPLEMENTARY NOTES	12. SPONSORING MILITARY ACTIVITY
Available in DDC.	Arnold Engineering Development Center, Air Force Systems Command, Arnold AF Station, Tennessee 37389.

13. ABSTRACT

The effects of thermal nonequilibrium (elevated electron temperature) and ionizational nonequilibrium (finite-rate recombination) are studied in the insulator boundary layer of a potassium-seeded nitrogen MHD accelerator flow. The nonsimilar, compressible boundary layer is assumed steady, laminar, and two-dimensional. A collisionless sheath is assumed and matched with the boundary layer equations, which are solved numerically for a core flow Hall-neutralized Faraday accelerator. The relative importance of the various terms in the electron energy equation are assessed, and the overall effect of the nonequilibrium phenomena on the boundary layer parameters is described. It is concluded that thermal nonequilibrium can lead to significant B-wall shorting in long channels and that Hall effects should not be neglected but that operation is not noticeably affected by ionizational nonequilibrium or the physics of the electrostatic sheath.

DD FORM 1 NOV 65 1473

UNCLASSIFIED

Security Classification

14. KEY WORDS	LINK A		LINK B		LINK C	
	ROLE	WT	ROLE	WT	ROLE	WT
magnetohydrodynamic generator						
magnetohydrodynamic accelerator						
boundary layer						
ionization						
nonequilibrium flow						

AFSC
Arnold AFS Tenn